Applied Thermal Engineering 302 (2026) 131692

Contents lists available at ScienceDirect

Applied Thermal Engineering

journal homepage: www.elsevier.com/locate/ate

Research Paper

Multistage solar-driven membrane distillation with direct ambient-temperature feed heating

Stefan Morosanu [a,b], Alessandro Monticelli [b], Matteo Morciano [a,c,*]

[a] Department of Energy, Politecnico di Torino, Corso Duca degli Abruzzi 24, 10129 Torino, Italy
[b] Green Independence S.R.L., Piazza del Popolo 1, 72100 Brindisi, Italy
[c] Clean Water Center, Politecnico di Torino, Corso Duca degli Abruzzi 24, 10129 Torino, Italy

ARTICLE INFO

Dataset link: https://zenodo.org/records/18242958

Keywords:
Thermal membrane distillation
Internal heat recovery
Solar energy
Renewable energy sources
Sustainability

ABSTRACT

Water scarcity is intensifying worldwide, driving the need for compact, energy-efficient desalination technologies suitable for decentralized and off-grid operation. This study aims to enhance freshwater productivity of solar-driven membrane distillation by developing and analyzing a multistage direct contact membrane distillation (DCMD) system powered solely by distributed solar energy under ambient-temperature feed conditions. The work extends a previously demonstrated single-stage concept to multistage operation without external feed preheating, active cooling, or solar concentration. Two system configurations are investigated: (i) a counter-current multistage system with external heat exchange for cooling, used as a benchmark, and (ii) a fully self-contained configuration relying exclusively on internal thermal management. A numerical model is developed and validated against experimental data, showing good agreement. An optimization algorithm is then employed to determine optimal feed and permeate mass flow rates and to assess the effects of stage number and solar irradiance. Results show that the externally cooled configuration exhibits an approximately linear increase in specific productivity with the number of stages, reaching 1.71 kg m^{-2} h^{-1} for four-stage configuration under 700 W m^{-2}. The configuration with internal heat recovery further enhances performance, achieving 2.33 kg m^{-2} h^{-1} and a gain output ratio of 1.58. Model extrapolation indicates potential productivity up to about 3 and 4 kg m^{-2} h^{-1} for seven-stage configuration at 700 and 1000 W m^{-2}, respectively, with emerging saturation effects. These results demonstrate that the proposed design enables higher freshwater production compared to state-of-the-art compact solar-powered MD systems, offering a scalable and energy-efficient solution for decentralized and off-grid desalination applications.

1. Introduction

Billions of people worldwide experience water scarcity for at least one month each year [1], a condition that is expected to worsen in the coming decades as a consequence of population growth, climate change, and increasing pressure on freshwater resources [2,3]. These trends underscore the urgent need for desalination technologies that are not only effective, but also sustainable [4], resilient, and suitable for deployment in decentralized and resource-constrained settings [5,6]. In this context, the integration of desalination processes with renewable energy sources [4,7] is widely recognized as a key strategy to reduce environmental impact while ensuring reliable access to potable water [8–10].

Among renewable resources, solar energy stands out for its abundance and global availability [11], while seawater constitutes the largest accessible water reservoir on Earth [12]. However, the relatively low power density of solar irradiation poses significant challenges when interfaced with conventional, energy-intensive desalination technologies. Recent advances in solar thermal technologies, including the use of advanced materials, hybrid nanofluids, and enhanced heat transfer structures, have demonstrated improved energy capture and storage performance [13]. However, their integration into compact and decentralized desalination systems remains limited. Membrane distillation (MD), a thermally driven separation process capable of operating with low-grade heat, has therefore emerged as a promising candidate for solar-driven desalination [14,15]. Over the past decade, numerous solar-powered MD systems have been reported [16], most of which rely on complex system architectures that include solar collectors, thermal storage units, heat exchangers, and auxiliary cooling loops. In parallel, recent studies have increasingly explored the role of MD within broader integrated water–energy systems. A representative example

* Corresponding author at: Department of Energy, Politecnico di Torino, Corso Duca degli Abruzzi 24, 10129 Torino, Italy.
E-mail address: matteo.morciano@polito.it (M. Morciano).

https://doi.org/10.1016/j.applthermaleng.2026.131692
Received 31 March 2026; Received in revised form 26 May 2026; Accepted 28 May 2026
Available online 10 June 2026
1359-4311/© 2026 The Authors. Published by Elsevier Ltd. This is an open access article under the CC BY license (http://creativecommons.org/licenses/by/4.0/).

is the growing interest in renewable hydrogen production, which is strengthening the link between water availability, water quality, and energy system integration [17]. The IEA Global Hydrogen Review 2024 [18] highlights that a significant share of planned low-emission hydrogen projects is located in water-stressed regions, where desalination and water reuse are emerging as enabling technologies. In this context, MD is relevant not only for freshwater production but also as a potential subsystem for supplying high-purity water to electrolyzers and for valorizing waste heat [17,19,20], as demonstrated by recent studies on PV/MD configurations and MD–electrolyzer integration [21]. The integration of desalination and hydrogen-production technologies enables multigeneration frameworks capable of simultaneously producing high-purity water, hydrogen, and useful thermal or electrical energy streams. Such integrated configurations may improve overall system efficiency through enhanced heat recovery and thermal integration, while also supporting compact and decentralized energy–water infrastructures [22]. These developments suggest that compact and integrated MD architectures are of interest not only for decentralized desalination, but more broadly for distributed water–energy systems. Although such configurations can achieve relatively high freshwater production rates, their complexity, footprint, and dependence on external components limit their applicability in compact, off-grid, or low-infrastructure scenarios.

To address these limitations, increasing attention has been devoted to compact and integrated solar-driven MD architectures, in which the solar absorber is directly incorporated into the desalination module [23,24]. Early developments in this direction have predominantly focused on passive [25,26], capillary-fed devices [27–29], enabling fully autonomous operation without external pumps. Notably, multistage capillary-based systems have demonstrated high specific productivity by reusing residual heat across successive stages [25,30]. Despite these encouraging results, the reliance on capillary transport imposes intrinsic geometric constraints: the maximum achievable device length is limited to approximately 10–16 cm [27,31], which restricts the usable membrane area and ultimately constrains the absolute freshwater production and scalability of such systems.

To overcome the size and throughput limitations of passive configurations, a number of active MD concepts have been proposed [32]. These systems can be broadly divided into photothermal [33–35] and non-photothermal active architectures. Photothermal MD devices incorporate solar-absorbing materials at or near the membrane surface to induce localized heating [36,37] and mitigate temperature polarization. While specific productivities in the range of 0.3–0.5 kg m^{-2} h^{-1} have been reported [38], higher values are often achieved using lab-scale photothermal coatings [34]. Moreover, photothermal approaches frequently rely on advanced coatings or nanostructured materials, raising concerns related to long-term durability, fabrication complexity, and large-scale manufacturability [39]. Non-photothermal active systems, on the other hand, typically exploit external waste-heat sources or require auxiliary cooling circuits. For example, photovoltaic-coupled air-gap MD configurations have been proposed [40], but their performance under varying operating conditions and their scalability remain insufficiently explored, and active cooling is still required [41]. As a result, active MD systems that operate exclusively using distributed solar energy absorbed directly along the feed channel, without feed preheating, solar concentration, photothermal coatings, or external cooling, remain remarkably underrepresented in the literature, particularly beyond single-stage operation.

In this context, Morosanu et al. [42] recently demonstrated the feasibility of a compact, single-stage DCMD module that directly harvests solar energy distributed along the feed channel. The system operates with ambient-temperature feedwater and relies on active circulation to ensure controlled thermal management, while avoiding external preheating, vacuum assistance, or photothermal functionalization. Under these low driving-temperature conditions, a specific productivity of 0.51 kg m^{-2} h^{-1} was achieved. A comparison with existing compact solar-driven MD systems showed that the overall productivity (evaluated in g h^{-1}) is comparable to that of both passive capillary-based devices and more complex photothermal architectures, while avoiding their respective limitations in terms of scalability, geometric constraints, and material complexity.

While this prior work established the viability and competitiveness of actively circulated, compact MD modules powered solely by distributed solar heat, it also revealed an intrinsic limitation associated with single-stage operation under low inlet temperatures: the limited driving temperature difference inherently constrains further gains in productivity and thermal efficiency. These observations indicate that extending such architectures to multistage configurations represents a crucial step toward enhancing freshwater production while preserving compactness, simplicity, and scalability [43,44]. At the same time, multistage operation under distributed solar heating introduces additional challenges related to heat distribution, inter-stage coupling, and flow management, which require careful design and optimization.

In this study, we extend the previously proposed single-stage concept [42] by investigating, for the first time, a multistage configuration of actively circulated, distributed-solar DCMD aimed at enabling stage-wise heat recovery. Two system layouts are considered: the first incorporates an external heat exchanger for cooling, whereas the second relies solely on internal thermal management. In the latter, the permeate stream from the final stage transfers heat to an auxiliary feed channel, thereby preheating the incoming feed. This configuration operates without external feed preheating or active cooling and is designed as a compact, scalable solution for off-grid applications. A combined experimental and numerical approach is employed to evaluate system performance, validate a predictive model, and systematically examine the effects of multistaging, flow rate optimization, and solar irradiance. The validated model is then used to investigate coupled heat and mass transfer across multiple stages, determine optimal feed and permeate flow rates, and quantify the influence of stage number on freshwater productivity and thermal efficiency. Finally, the model is applied to extrapolate system performance beyond experimentally accessible conditions and configurations and to benchmark the proposed multistage architecture against the current state of the art, providing quantitative insights into its scalability and design potential.

2. Methodology

2.1. Description of the designed prototype

The prototype investigated in this study builds upon the compact, solar-driven MD architecture previously developed and characterized in our recent work [42]. In both cases, the system adopts a flat-sheet membrane configuration with distributed heating along the feed side. However, while the previous device was limited to a single-stage layout, the present work introduces and focuses on a multistage module designed to systematically explore performance gains enabled by staged operation and internal heat recovery.

Fig. 1(a) illustrates the main components of the prototype. The module consists of alternating feed and permeate channels stacked on top of each other, with the total number of channels determined by the number of stages installed (see Fig. 1b). Each channel has a height of 2.6 mm. Between each feed–permeate channel pair, a hydrophobic polytetrafluoroethylene (PTFE) membrane is placed, with a thickness of 0.18 mm, a porosity of 0.825, and an average pore size of 0.45 μm.

The overall footprint ($A_{\text{footprint}}$) of the module is 46 × 46 cm^2, while the effective membrane area (A_m) is 39 × 39 cm^2. In this work, the solar collector area coincides with the footprint area, i.e. $A_c = A_{\text{footprint}}$. All specific productivity values reported for both the numerical and experimental results are referred to the effective membrane area A_m.

The thermal gradient driving vapor transport is induced by an electric heater (heating mat) placed on the top surface of the device,

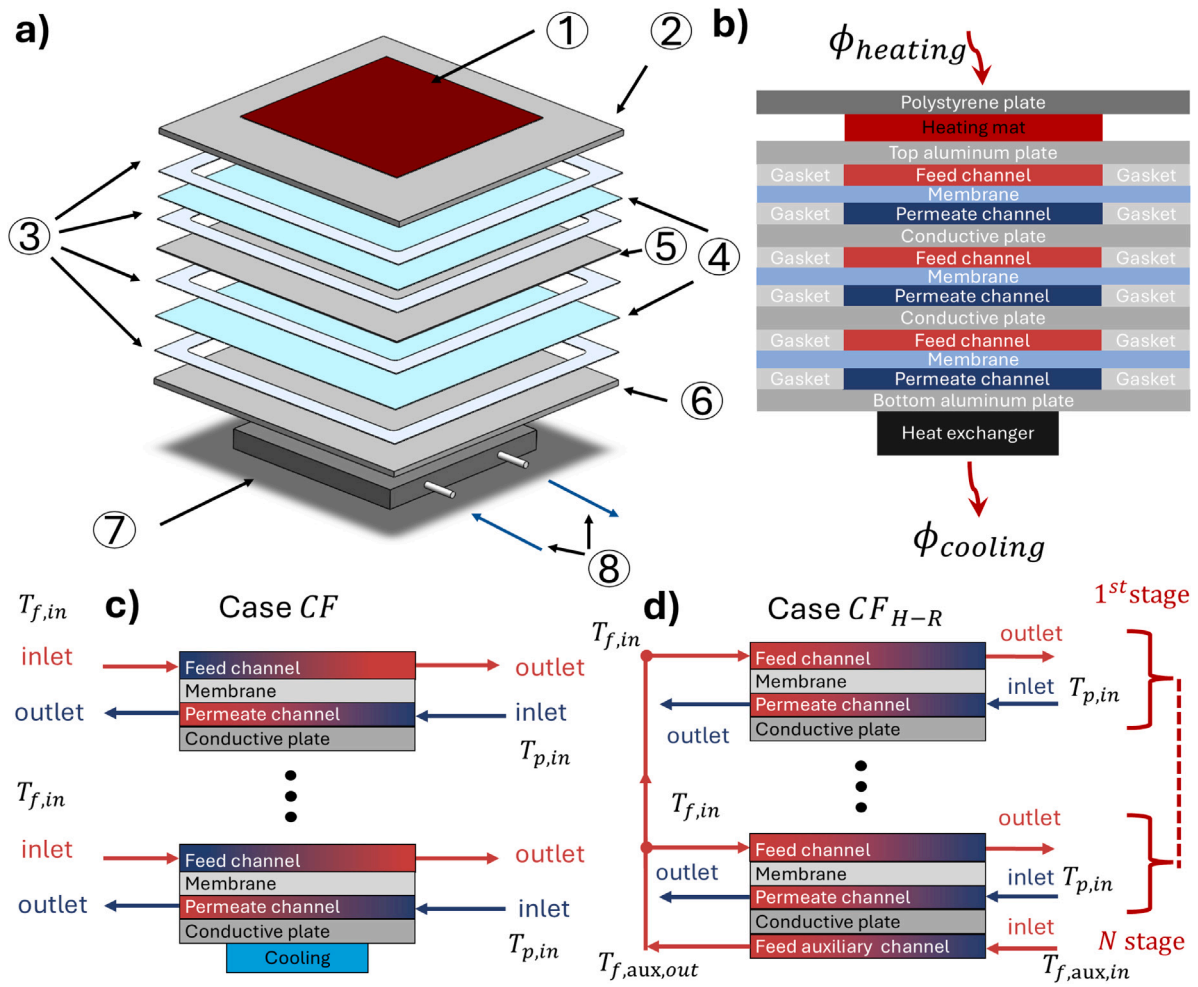


Fig. 1. Schematic representation of the main device components and layouts. (a) CAD model of a two-stage configuration (CF), showing: (1) heating mat, (2) top aluminum plate, (3) sealing gasket, (4) membrane, (5) conductive plate, (6) bottom aluminum plate, (7) heat exchanger, and (8) inlet/outlet for the cooling fluid. (b) Cross-sectional view of a three-stage configuration device. (c) Schematic of the reference counter-current configuration (Case CF). (d) Schematic of the configuration with internal heat recovery (Case CF_{H-R}).

which emulates distributed solar irradiation over the entire footprint. The reduced channel height enhances heat transfer from the top (hot) side to the bottom (cold) side of the module, increasing the effective transmembrane temperature gradient and consequently the distillate flux. On the back side of the module, either an external heat exchanger (active cooling mode) or an internally integrated feed auxiliary channel (self-cooling mode) is used to remove heat from the permeate side, depending on the configuration under investigation, as schematically depicted in Fig. 1(c) and (d), respectively.

In this context, multistage refers to a configuration in which multiple stages — each consisting of a feed channel, a permeate channel, and a membrane — are connected in series and arranged in a vertically stacked layout. The stages are thermally coupled through a thin 2-mm aluminum plate that enables heat transfer from the permeate side of one stage to the feed side of the subsequent stage.

In the self-cooling configuration, the device does not rely on an external heat exchanger. An auxiliary feed channel placed beneath the permeate channels of the last stage functions simultaneously as a heat sink for the permeate and as a preheater for the incoming feed, enabling internal heat recovery and improving thermal utilization. The following subsection provides a detailed description of the two layouts and operating configurations considered.

2.1.1. Device layouts and operating configurations

In this work, two multistage DCMD layouts relying solely on distributed heating are investigated. In all configurations, the inlet feed temperature ($T_{f,in}$ or $T_{f,\mathrm{aux},in}$ depending on the configuration; see Fig. 1c,d), the permeate inlet temperature ($T_{p,in}$), and the ambient temperature (T_{amb}) were set to 20 °C. When present, the heat-sink temperature (T_{sink}) was also fixed at 20 °C. The stages are numbered from top to bottom, with the first stage located closest to the electric heater or solar collector.

- CF: counter-current flow configuration with external heat exchanger (see Fig. 1c). In this configuration, the feed and permeate streams flow in opposite directions through the stacked stages. This flow arrangement represents the state-of-the-art layout for conventional DCMD systems and is here extended to a multistage, distributed-heating context. In detail, heat is only supplied from the top side by distributed solar-like heating, while an external heat exchanger in contact with the bottom plate provides active cooling on the permeate side.
- CF_{H-R}: counter-current flow configuration with internal heat recovery (see Fig. 1d). In this layout, the total incoming feed stream ($\dot{m}_{f,\mathrm{tot}}$) is routed, prior to entering the stages, through an auxiliary channel positioned behind the final permeate channel and separated by a thin aluminum plate. The total feed mass flow rate ($\dot{m}_{f,\mathrm{tot}}$) is then uniformly distributed among the feed channels of each stage, as in the CF configuration. This arrangement enables heat exchange between the warm permeate exiting the last stage and the incoming feed at ambient temperature, thereby

recovering heat that would otherwise be rejected to an external sink. As a result, the feed is preheated while the permeate is simultaneously cooled, increasing the feed temperature before it enters the stages and contacts the active membrane area. No external heat exchanger or chiller is required on the permeate side; the device thus operates as a self-contained, internally heat-recovered multistage module.

In both configurations, the nominal membrane area per footprint is kept constant, so that changes in performance can be directly attributed to the number of stages and to the different thermal architectures (external vs. internal heat recovery), rather than to variations in collector size or active exposed area.

2.2. Experimental setup

The experimental setup used for the validation of the numerical model is shown in Fig. 2. The system was designed to evaluate the specific mass flow rate of distilled water through the membrane, referred to as the permeate flux J, expressed in kg m^{-2} h^{-1}. Configuration CF was considered.

In all experiments, a target solar-equivalent irradiance of 1 sun was reproduced by applying a distributed heat flux of $\phi_{\text{heating}} = 700$ W m^{-2}. This value was selected to account for heat losses, assuming a realistic 30% loss [42]. For practical reasons, a smaller silicone heating mat (RS Components) was used instead of heating the entire collector area ($A_{\text{footprint}}$). The electrical power supplied to the mat was adjusted to reproduce a solar-equivalent heat flux of 700 W m^{-2} over the device footprint. The heater was powered and controlled by a DC power supply (EA-PS 3200-10 C), allowing precise control of the energy input. A polystyrene plate was placed on top of the heating mat to thermally insulate it from the environment and to ensure that the supplied heating power was effectively delivered to the device.

The feed salinity was set at 35 g L^{-1}, and the inlet temperatures of both the feed ($T_{f,in}$) and permeate ($T_{p,in}$) streams were maintained at 20 °C. When testing configuration CF, the bottom plate of the device was cooled by circulating a cooling fluid through an external heat exchanger. The thermostatic bath (Julabo Corio CD-300F) regulated all three temperatures — the feed inlet, the permeate inlet, and the cooling fluid (both upstream and within the heat exchanger) — ensuring constant values of T_{sink}, $T_{f,in}$ and $T_{p,in}$ equal to 20 °C throughout the tests.

The mass flow rates in the feed ($\dot{m}_f$) and permeate ($\dot{m}_p$) loops were regulated using a proportional valve (Dolphin Fluid) and monitored with a flow meter (Digmesa). In this work, $\dot{m}_f$ and $\dot{m}_p$ are defined as the mass flow rates through a single feed channel and a single permeate channel, respectively (i.e., per semi-stage). Since each stage consists of one feed channel and one permeate channel, the total feed and permeate mass flow rates of the device scale with the number of stages as $\dot{m}_{f,\text{tot}} = \dot{m}_f N_{\text{stage}}$ and $\dot{m}_{p,\text{tot}} = \dot{m}_p N_{\text{stage}}$, respectively. The circulation was driven by a gear pump (Fluid-o-Tech). The permeate flux J was determined by measuring the mass variation of the permeate basin over time using a precision balance (Radwag PS 1000.R2). To verify mass conservation, the feed basin was also monitored with a precision balance (Kern PCB). Finally, to evaluate water quality and detect potential salt leakage, the permeate conductivity was continuously monitored using a conductivity meter (Chauvin Arnoux C.A 10141).

2.2.1. Experimental procedure

All experiments were conducted following a standardized procedure to ensure consistent and repeatable testing conditions across configurations and stage numbers. First, the permeate channels were filled with distilled water and the feed channels with artificial seawater at a salinity of 35 g L^{-1}. Once the module was fully filled and all hydraulic connections were checked, the DC power supply was switched on and the heating mat set to the desired power.

After approximately 30–60 min of continuous heating and circulation, the system reached steady-state operation, as confirmed by the stabilization of inlet/outlet temperatures and of the permeate production rate. Once steady state was attained, the experiment was continued for an additional 90 min, resulting in a total test duration of approximately 2–2.5 h.

Throughout the entire test, $T_{f,in}$, $T_{p,in}$, and, when present, T_{sink} were maintained at 20 °C using the thermostatic bath. Permeate mass, feed mass, and permeate conductivity were continuously recorded for subsequent analysis and comparison with the numerical model. To ensure repeatability of the prototype's performance, each test was repeated at least three times.

2.3. Numerical model

To analyze the performance of the multistage prototype, gain a comprehensive understanding of its behavior, and enable reliable extrapolation beyond experimentally tested conditions, a numerical model was developed using the Finite Element Method (FEM) in COMSOL Multiphysics. The model is two-dimensional and assumes steady-state conditions, representing a cross-section of the device that includes all feed and permeate channels, the membranes, and the conductive components (i.e., top and bottom plates and intermediate aluminum layers), as shown in Fig. 3. The spacers are not explicitly modeled. As discussed in our previous work [42], neglecting the spacers leads to a small and conservative underestimation of productivity under the low-flow laminar regime considered here.

The present model extends the single-stage framework previously developed and validated in Ref. [42]. The same governing equations, thermophysical properties, and membrane transport relations are retained. The main novelties introduced in this work are: (i) the inclusion of multiple stacked stages, and (ii) the thermal coupling between stages. For completeness, a concise summary of the key equations is provided below, while full derivations and additional details are available in Ref. [42].

2.3.1. Main governing equations

Fluid flow in the feed and permeate channels is described by the steady-state Navier–Stokes equations for an incompressible fluid [45]:

$$\rho \vec{u} \cdot \nabla \vec{u} = -\nabla p + \mu \nabla^2 \vec{u} + \mathbf{f}, \tag{1}$$

where $\vec{u}$ is the fluid velocity vector, p the pressure, μ the dynamic viscosity, ρ the density and $\mathbf{f}$ the body force per unit volume. Considering the low mass flow rates, the flow regime is laminar, with Reynolds numbers on the order of 10 for the maximum simulated flow rate.

Heat transfer in the channels and solid domains (excluding the porous membrane region) is governed by the steady-state energy equation [45]:

$$\vec{u} \cdot \nabla T = \frac{k}{\rho c_p} \nabla^2 T + \frac{q}{\rho c_p}, \tag{2}$$

where T is the temperature, k the thermal conductivity, c_p the specific heat, and q a volumetric heat source term.

In the feed channels, salt transport is modeled using the steady-state advection–diffusion equation [30]:

$$\vec{u} \cdot \nabla c = D \nabla^2 c + S, \tag{3}$$

where c is the salt concentration, D the molecular diffusion coefficient of NaCl in water, and S a source/sink term related to local concentration changes induced by evaporation at the membrane interface.

These equations, together with the membrane transport relations summarized below, are aligned with those adopted in Ref. [42] and are only briefly recalled here for clarity.

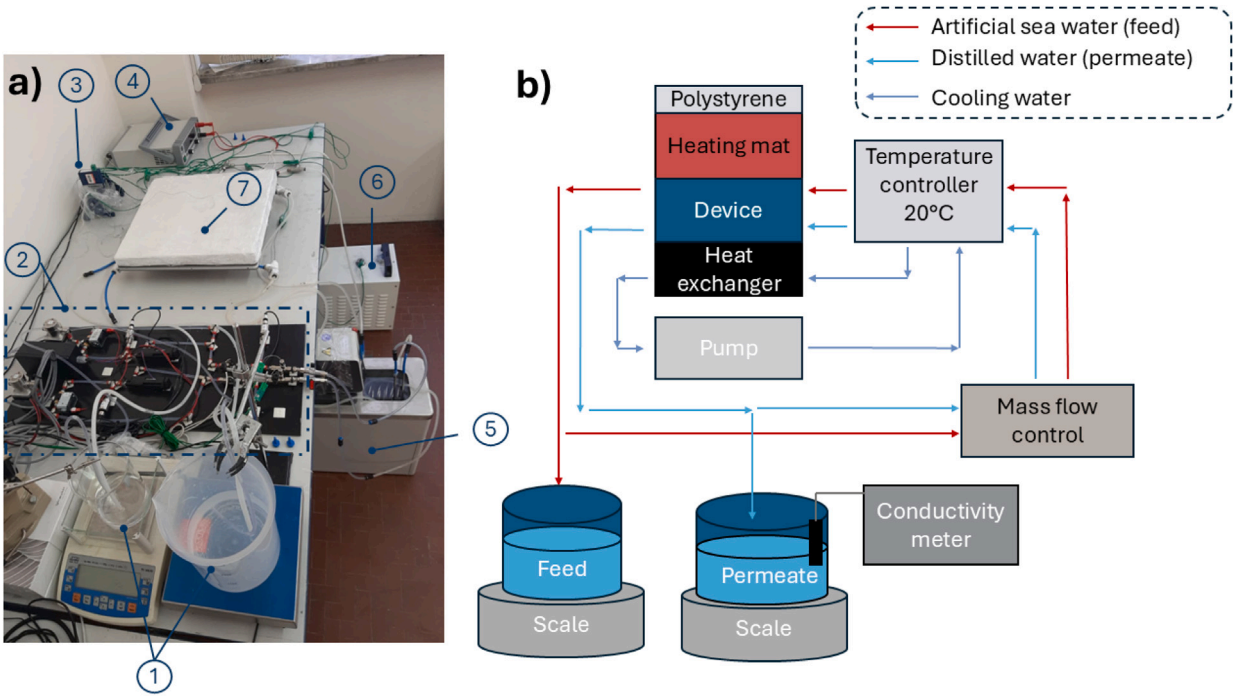


Fig. 2. Experimental setup used for the validation of the numerical model. (a) Photograph of the physical setup, with numbering indicating the main components: (1) feed and permeate basins, (2) pumping hardware for precision mass flow rate control, (3) data acquisition system, (4) DC power supply, (5) thermal bath for temperature control, (6) chiller, (7) device covered with a polystyrene insulating layer. (b) Schematic illustration of the main components and hydraulic connections of the experimental setup.

2.3.2. Mass transfer across the membrane

Mass transfer through the membrane is modeled using the same Maxwell–Stefan and Dusty-Gas framework adopted in Ref. [42], under the assumptions of negligible total pressure gradient, binary gas mixture (water vapor and air), and ideal gas behavior. Under these assumptions, the final expression for the specific mass flux J across the membrane can be written as:

$$J = K\,\Delta p_v, \tag{4}$$

where Δp_v is the difference in water vapor pressure between the two membrane surfaces and K is the effective permeability of the porous membrane. The permeability is given by:

$$K = \left(\frac{RT\,p_a\,\tau\,h}{\epsilon\,M_{\mathrm{H_2O}}\,p\,D_{wa}} + \frac{RT\,\tau\,h}{\epsilon\,M_{\mathrm{H_2O}}\,D_{wK}\,d_p} \right)^{-1}, \tag{5}$$

where R is the gas constant, p_a the partial pressure of air, ϵ the membrane porosity, τ the tortuosity, h the membrane thickness, d_p the average pore diameter, D_{wa} the binary diffusion coefficient of water vapor in air, and D_{wK} the Knudsen diffusion coefficient (see Refs. [25,30,42] for the full derivation).

The driving force is defined as:

$$\Delta p_v = \alpha(Y_F)\,p_v(T_F) - \alpha(Y_P)\,p_v(T_P), \tag{6}$$

where $p_v(T)$ is the vapor pressure of pure water at temperature T, evaluated via Antoine's correlation, and $\alpha(Y)$ is the water activity. The latter is computed from the salt mass fraction Y using [25]:

$$\alpha = \frac{M_{\mathrm{NaCl}}(1-Y)}{M_{\mathrm{NaCl}}(1-Y) + N_{\mathrm{ion}}M_{\mathrm{H_2O}}Y}, \tag{7}$$

with M_{NaCl} and $M_{\mathrm{H_2O}}$ denoting the molar masses of NaCl and water, respectively, and N_{ion} the number of ions per salt molecule.

2.3.3. Heat transfer across the membrane

Heat transfer through the membrane accounts for both conduction and phase-change contributions. The total heat flux ϕ is expressed as [46]:

$$\phi = \frac{k_m}{h}\Delta T + J\,\Delta h_v, \tag{8}$$

where ΔT is the temperature difference across the membrane, Δh_v is the latent heat of vaporization, and k_m is the effective thermal conductivity of the membrane, evaluated as:

$$k_m = (1-\epsilon)\,k_{PTFE} + \epsilon\,k_{air}, \tag{9}$$

with k_{PTFE} the thermal conductivity of the polymer matrix and k_{air} that of the air trapped in the pores. This formulation is the same as in Ref. [42].

2.3.4. Boundary conditions and multistage coupling

The main boundary conditions applied to the computational domain are shown in Fig. 3 for the reference counter-current configuration (CF). Inlet temperatures $T_{p,in}$ and $T_{f,in}$ are imposed via realistic heat-flux boundary conditions (i.e., $\phi = \dot{m}_{in}\int_{T_{in}}^{T} c_p\,dT$), while the mass flow rates per stage, $\dot{m}_p$ and $\dot{m}_f$, are imposed at the corresponding inlets (i.e., $\dot{m}_{\mathrm{in}} = \int_{\partial\Omega}\rho\,(\vec{u}\cdot\hat{n})\,ds$, where ds represents an infinitesimal element of the inlet surface). Standard outflow conditions are applied at each stage outlet for mass, momentum, and energy.

The computational domain considers an area of 40 × 39 cm^2, corresponding to the channel footprint. This is slightly larger than the active membrane area (by 2.5%) due to the presence of sealing gaskets that cover a small portion of the membrane. For consistency with the real prototype, the active membrane area is maintained at 39 × 39 cm^2, while the remaining portion included in the numerical domain does not contribute to mass transfer. Consequently, the simulations focus on the channel footprint.

In the reference configuration with external heat exchanger (CF), the bottom plate is cooled by a prescribed heat flux boundary condition of the form $\phi_{\mathrm{sink}} = U_{\mathrm{sink}}(T - T_{\mathrm{sink}})$, where U_{sink} is taken from the experimental characterization. In particular, the heat exchanger is modeled with $U_{\mathrm{sink}} = 125$ W m^{-2} K^{-1}. T_{sink} denotes the temperature of

the cooling fluid in the heat exchanger located on the backside of the prototype (see Fig. 1). In the configuration with internal heat recovery (CF_{H-R}), the external heat exchanger is removed and replaced by an auxiliary feed channel located beneath the last permeate channel. In this arrangement, the total feed mass flow rate, $\dot{m}_{f,\mathrm{tot}} = \dot{m}_f N_{\mathrm{stage}}$, first passes through the auxiliary channel, where it exchanges heat with the warm permeate, before entering the stacked feed stages. The outlet temperature of the auxiliary channel, $T_{f,\mathrm{aux},out}$, is then used as the inlet temperature for the feed entering the stacked stages, i.e., $T_{f,in} = T_{f,\mathrm{aux},out}$ (see Fig. 1d). This assumption may lead to a slight underestimation of the actual feed inlet temperature, as the fluid may undergo marginal preheating while flowing through the short connection channels between successive stages. However, this effect is limited by the small characteristic length of these channels (on the order of a few centimeters) and by the relatively high flow velocity, which results in a short residence time. As a consequence, the heat absorbed by the fluid in these regions is minimal compared to the dominant heating occurring within the solar collector, where velocities are lower, considering mass flow rate conservation, and heat transfer is more effective. Therefore, the associated preheating effect can be considered negligible, and the assumption is conservative with respect to the prediction of the main performance indicators [42]. Moreover, a 2 mm-thick aluminum plate separates the auxiliary feed channel from the permeate side, facilitating heat exchange between the permeate exiting the final stage and the incoming feed. This internal heat-recovery loop eliminates the need for an external heat exchanger, enabling self-cooling and improving overall thermal efficiency. As in CF, heat losses from the external surfaces are modeled via convective heat transfer to the environment. Heat transfer from the module to the surrounding environment is modeled as $\phi = U_{\mathrm{amb}}(T - T_{\mathrm{amb}})$, where $T_{\mathrm{amb}} = 25$ °C is the ambient temperature and $U_{\mathrm{amb}} = h_{\mathrm{air}}$, with $h_{\mathrm{air}} = 5$ W m^{-2} K^{-1} representing the natural convection coefficient.

The top surface includes both the thermal power input from the electric heater and convective losses to the ambient, and is modeled as $\phi = F_c\,\phi_{\mathrm{heating}} - U_{\mathrm{loss}}(T - T_{\mathrm{amb}})$. Here, the coefficient F_c accounts for the difference between the solar collector area ($A_{footprint}$) and the area used in the numerical model (40 × 39 cm^2), ensuring that the total incident power is consistent with the experimental conditions. Since a polystyrene insulating plate is placed on top of the prototype, the effective heat transfer coefficient U_{loss} is expressed as $U_{\mathrm{loss}} = \left(\frac{1}{L_p/k_p} + \frac{1}{h_{\mathrm{air}}}\right)^{-1}$, where $L_p = 2$ cm is the thickness of the polystyrene plate and $k_p = 0.031$ W m^{-1} K^{-1} its thermal conductivity.

For clarity, the boundary conditions for the advection–diffusion equation governing salt transport in the feed channels are not shown in Fig. 3. At the inlet of each feed channel, the salt concentration is set to 35 g L^{-1}. At the membrane interface, a boundary condition is imposed to account for salt accumulation due to evaporation, with the salt flux obtained from the vapor flux via a local mass balance. On all remaining solid boundaries, a no-flux condition is applied.

2.4. Feed and permeate mass flow rate optimization

The feed ($\dot{m}_f$) and permeate ($\dot{m}_p$) mass flow rates per stage are key control parameters in the active multistage configuration. To assess system performance under different heating fluxes (ϕ_{heating}) and numbers of stages, a derivative-based optimization algorithm was implemented to determine the optimal per-stage mass flow rates within predefined bounds for both the feed and permeate channels. Derivative-based methods are well-suited here, as the objective function — the transmembrane distillate flux — is smooth and exhibits a single well-defined maximum within the operating range of interest. The algorithm determines the optimal feed mass flow rate for each permeate flow under each operating condition, i.e., for every combination of heating flux, stage number, and thermal configuration (external heat exchanger vs. internal heat recovery). This yields the optimal per-stage mass flow rate for each scenario, allowing a consistent comparison of the benefits of multistage operation and internal heat recovery.

3. Results

3.1. Main experimental results

The first configuration investigated was the counter-current flow arrangement (CF), which is widely reported in the literature as the most promising fluidic layout for membrane distillation systems. This configuration was also selected for the validation of the numerical model.

The prototype was tested under a distributed heat flux of 700 W m^{-2}, using artificial seawater with a salinity of 35 g L^{-1}. $T_{f,in}$ and $T_{p,in}$ were both set to 20 °C, while the heat sink temperature (T_{sink}) was maintained at 20 °C. The selected heat flux value is representative of realistic solar irradiance levels under typical operating conditions, making it suitable for both experimental assessment and model validation.

The experimental results demonstrate that the multistage configuration significantly enhances the specific distillate productivity (J). As shown in Fig. 4 (see red circles), increasing the number of stages from one to three leads to an almost linear increase in J, rising from approximately 0.43 ± 0.02 to 0.75 ± 0.02 kg m^{-2} h^{-1}, and further up to 1.29 ± 0.02 kg m^{-2} h^{-1}. When a fourth stage is added, the productivity reaches 1.57 ± 0.03 kg m^{-2} h^{-1}, which is slightly lower than the linear extrapolated value of 1.71 kg m^{-2} h^{-1}. This deviation indicates the onset of performance saturation, likely due to diminishing temperature driving forces across successive stages. To better assess the energetic performance of the system, the thermal efficiency is expressed in terms of the Gain Output Ratio (GOR), defined as $GOR = \frac{J A_{\mathrm{m}} \Delta h_{\mathrm{v}}}{\phi_{\mathrm{heating}} A_{\mathrm{footprint}}}$. For multistage configurations, GOR is more appropriate than stage-wise thermal efficiency, as it reflects the overall system performance by accounting for the reuse of thermal energy across successive stages. Accordingly, GOR reaches values of about 110% for the four-stage configuration. The specific thermal energy consumption ($STEC$), expressed as $STEC = \frac{\phi_{\mathrm{heating}} A_{\mathrm{footprint}}}{J A_{\mathrm{m}}}$, decreases from 2264 kWh$_{\mathrm{th}}$ m^{-3} for the single-stage configuration to 620 kWh$_{\mathrm{th}}$ m^{-3} for the four-stage configuration. This result is particularly noteworthy considering that the present design is intended for scalable, medium-area implementations and does not rely on capillary-driven transport mechanisms commonly adopted in previously reported laboratory-scale systems powered by distributed energy. An additional outcome of the experimental campaign concerns the quality of the produced water. The electrical conductivity of the permeate, monitored as an indicator of salt rejection performance, remained consistently low across all tested configurations, with an average value of 27 ± 12 μS cm^{-1}, where the uncertainty represents one standard deviation. This value was calculated after excluding the initial volume of distillate collected at the start of each experiment, in order to eliminate potential dilution effects and ensure a consistent assessment of permeate quality. The absence of any systematic increase in electrical conductivity with the number of stages indicates negligible salt leakage or carryover, thereby confirming the integrity of the sealing and the overall reliability of the experimental setup.

3.2. Validation of the numerical model

The validation of the numerical model is presented in Fig. 4, where the numerical predictions are directly compared with the experimental results for the CF configuration. The main sources of uncertainty in the numerical model arise from variations in membrane properties, particularly porosity and thickness, while other factors, such as temperature, heating flux, and mass flow rate within the investigated operating range, exert a comparatively minor influence on the predicted distillate productivity. For instance, when a numerical uncertainty of ±2 °C is applied simultaneously to the three main temperatures of the system ($T_{f,in}$, $T_{p,in}$, and T_{sink}), the resulting variation in J is approximately ±5%, assuming fixed membrane porosity and thickness. Furthermore,

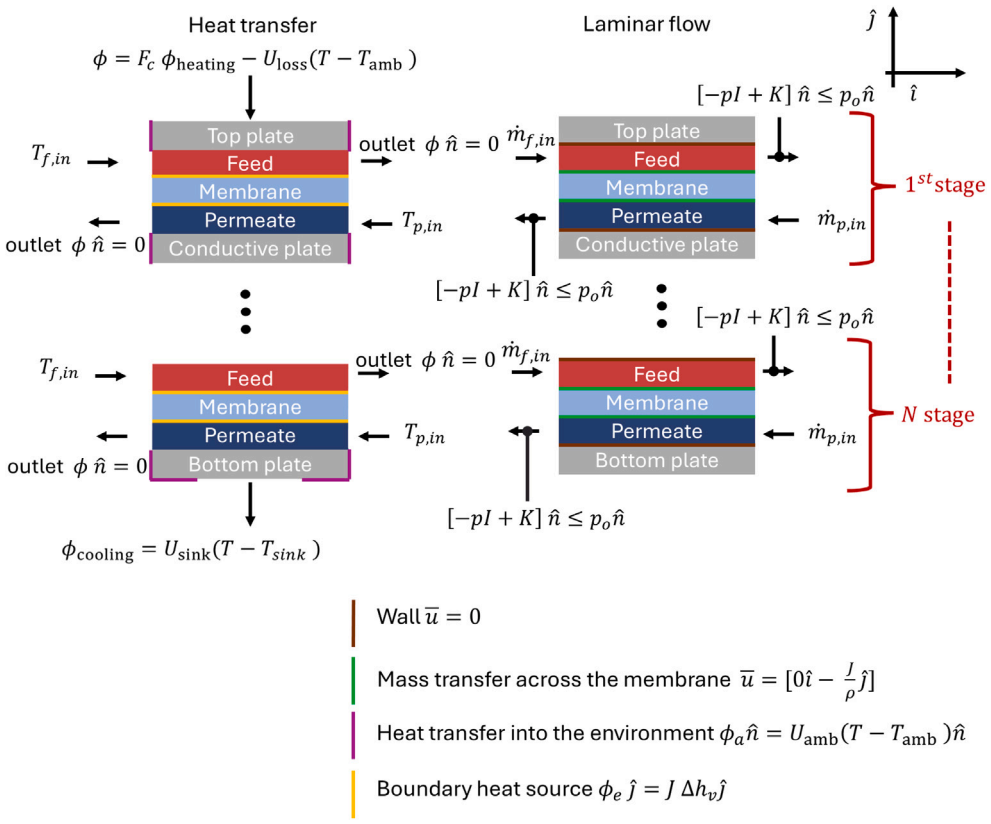


Fig. 3. Schematic representation of the boundary conditions used in the numerical model for configuration CF (validation case). Dark purple lines indicate heat losses to the environment, orange lines represent evaporation boundary heat sources, and green lines mark membrane–stream interfaces where vapor transfer occurs.

uncertainties in mass flow rate and heating flux (within the experimental ranges considered) lead to variations in J below 2%. In contrast, when temperature, mass flow rate, and heating flux are fixed at their nominal values and the uncertainty is attributed to variations in membrane porosity and thickness, the predicted variation in J increases to approximately ±25%. Consequently, only uncertainties related to membrane properties were considered in the validation analysis. Overall, the numerical model shows strong agreement with the experimental measurements, with a maximum absolute deviation of approximately 14% and a MAPE (Mean Absolute Percentage Error) of about 9%. The high coefficient of determination ($R^2 = 0.98$) further confirms the excellent correlation between numerical and experimental results across all tested configurations. The prototype was tested with one to four installed stages. The per-stage feed and permeate mass flow rates ($\dot{m}_f$ and $\dot{m}_p$) were set to 20, 10, 6.67, and 6.25 mL min^{-1} for the one-, two-, three-, and four-stage configurations, respectively. These values were selected to ensure stable operation of the experimental setup, as the instrumentation showed reduced reliability at overall flow rates below approximately 20 mL min^{-1}. For configurations with a higher number of stages, the total flow rate was adjusted to avoid excessively low per-stage values. In the two-stage configuration, the model slightly over-predicts the experimental productivity by approximately 2%, whereas for all other configurations it slightly underpredicts the measured values. Nevertheless, all deviations remain within an acceptable range for engineering design and performance assessment. To ensure repeatability, each experiment was performed at least three times, and the results are reported with statistical uncertainty as ± one standard deviation, reflecting a statistical variation of approximately 5% among repeated experiments under identical operating conditions. The measurement uncertainty associated with J is negligible (below 0.01%) due to the high precision of the balance and is therefore not included in the error bars.

3.3. Configuration CF

The CF configuration was further investigated through a detailed numerical analysis using the validated model, with the aim of elucidating the underlying physical mechanisms governing the multistage system behavior. All simulations were performed under reference operating conditions representative of the experimental campaign: a distributed heat flux of 700 W m^{-2}, artificial seawater salinity of 35 g L^{-1}, and feed, permeate, and heat sink temperatures set to 20 °C.

Fig. 5a shows the specific distillate productivity, J, as a function of the mass flow rate for configurations with 1–4 installed stages. The first key observation is that the maximum achievable productivity increases with the number of stages, confirming the effectiveness of the multistage architecture. Notably, the optimal mass flow rate remains approximately constant across all configurations, with peak productivity occurring at $\dot{m}_f = \dot{m}_p = 3.5 \pm 1.5$ mL min^{-1}. This indicates that each stage has an intrinsic optimal operating condition that is largely independent of the total number of stages.

When the mass flow rate falls below the optimal value, further reductions continue to increase the mean membrane temperature. However, this increase does not compensate for salt accumulation on the membrane, which reduces the effective vapor pressure difference. At very low flow rates, the fraction of water that evaporates becomes significant relative to the total inflow, leading to a pronounced increase in solute concentration and a corresponding reduction in vapor pressure.

Conversely, increasing the mass flow rate above the optimal value also results in a progressive reduction of J due to decreases in both the mean membrane temperature and the thermal gradient across the membrane. This effect becomes more pronounced as the number of stages increases. For example, in the single-stage configuration, raising the mass flow rate from 3.5 to 20 mL min^{-1} decreases productivity by only 12%, whereas the same increase causes a 45% reduction in the

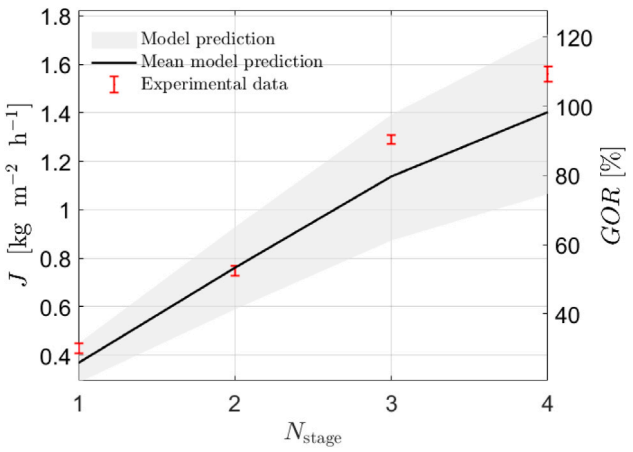


Fig. 4. Validation of the numerical model for the counter-current configuration (*CF*). The system was operated with artificial seawater (35 g L^{-1}) under a heating flux of 700 W m^{-2}. The feed and permeate inlet temperatures ($T_{f,in}$ and $T_{p,in}$) and a heat sink temperature (T_{sink}) were all set to 20 °C. The primary *y*-axis reports the specific distillate productivity *J* (kg m^{-2} h^{-1}) as a function of the number of stages (x-axis), while the secondary *y*-axis shows the corresponding Gain Output Ratio (*GOR*). The gray shaded region denotes the uncertainty band of the numerical predictions, associated with variations in membrane porosity (0.80–0.85) and thickness (0.13–0.23 mm). Experimental data are shown as red markers with statistical uncertainties (±std), while the solid black line represents the mean numerical prediction. Results were obtained assuming $\dot{m}_f = \dot{m}_p$. The mass flow rates were adjusted according to the number of stages and set to 20, 10, 6.7, and 6.25 mL min^{-1} for the one-, two-, three-, and four-stage configurations, respectively.

four-stage configuration. This pronounced sensitivity arises from the cumulative increase in total circulating mass flow ($\dot{m}_f N_{stage} + \dot{m}_p N_{stage}$) in multistage arrangements. At equal input thermal energy, the higher flow lowers the average fluid temperature across the system, significantly reducing the overall driving force for vapor transport. Based on these considerations, subsequent analyses (reported in Fig. 5b, c) focus on a mass flow rate of 3.5 mL min^{-1} ($\dot{m}_f = \dot{m}_p$), which provides a robust compromise between productivity maximization and operational stability.

Fig. 5b shows the contribution of each stage to the total specific distillate productivity as the number of stages increases. Notably, the productivity of the first stage increases from 0.42 kg m^{-2} h^{-1} in the single-stage configuration to 0.54 kg m^{-2} h^{-1} in the four-stage configuration. This enhancement is attributed to a higher mean membrane temperature ($\overline{T_m}$) experienced by the first stage in multistage arrangements (see Fig. 5c, showing mean membrane temperature and mean temperature difference across the membrane). Physically, this occurs because active external cooling is applied at the bottom of the device; increasing the number of stages enlarges the distance between the first and last stages, leading to a higher temperature level in the upstream stages. Specifically, in the single-stage configuration, the mean membrane temperature is approximately 34.1 °C, whereas in the four-stage configuration it reaches about 52.6 °C for the first stage (Fig. 5c). Although the mean temperature difference across the membrane ($\overline{\Delta T_m}$) decreases slightly with the number of stages, from 1.6 °C to 1.3 °C, the higher mean temperature more than compensates, resulting in a net increase in vapor flux. A similar trend is observed for the second stage, whose productivity rises from 0.37 kg m^{-2} h^{-1} in the two-stage configuration to 0.44 kg m^{-2} h^{-1} in the four-stage system.

Finally, Fig. 5b also shows the progressive reduction in productivity from the first to the last stage within each multistage configuration. For example, in the three-stage system, the mean membrane temperature decreases from 47.6 °C in the first stage to 31.9 °C in the last stage, while the mean transmembrane temperature difference remains nearly constant at 1.36 ± 0.04 °C (Fig. 5c). This monotonic decline in absolute temperature explains the lower productivity observed in downstream stages and highlights the dominant role of absolute temperature levels, rather than the temperature difference alone, in determining the performance of multistage membrane distillation systems.

3.4. Configuration CF_{H-R}

CF_{H-R} configuration was investigated exclusively through numerical simulations using the previously validated model. This configuration represents a proof-of-concept self-contained system that does not require external active cooling. Indeed, it does not rely on an external heat exchanger, with thermal regulation (cooling) achieved solely through control of the circulating mass flow rate.

All simulations were performed under reference operating conditions identical to those adopted for *CF*, namely a distributed heat flux of 700 W m^{-2}, an inlet salinity of 35 g L^{-1}, and feed and permeate inlet temperatures set to 20 °C. Equal mass flow rates were imposed in the feed and permeate channels ($\dot{m}_f = \dot{m}_p$), while the value was adjusted depending on the number of installed stages. In this configuration, the mass flow rate not only affects the hydrodynamic behavior but also directly controls the average system temperature, providing an additional degree of freedom for performance optimization. Indeed, since no external cooling mechanism is present, excessively low mass flow rates may lead to an uncontrolled temperature rise. Consequently, the numerical analysis was restricted to operating conditions for which the maximum temperature within the computational domain remained below 85 °C. This limitation was not required for *CF*, where the external heat exchanger constrains the maximum operating temperature.

Fig. 6a shows the specific distillate productivity, *J*, as a function of the mass flow rate for configurations with 1–4 installed stages. Unlike *CF*, the optimal per-stage mass flow rate strongly depends on the number of installed stages. The maximum productivity is achieved at approximately $\dot{m}_f = \dot{m}_p$ = 15, 7.5, 5, and 4 mL min^{-1} for one- to four-stage configurations, respectively. This trend reflects the fact that a total feed mass flow rate of approximately $\dot{m}_{f,tot}$ = 15 mL min^{-1} (i.e., $\dot{m}_{f,tot} = \dot{m}_f N_{stage} \approx 15$ mL min^{-1}) is required to ensure effective thermal regulation of the system; the same applies to the total permeate flow. As a result, the per-stage mass flow rate must decrease as the number of stages increases in order to maintain a comparable total flow, cooling capacity and, consequently, a similar thermal regulation of the system (e.g., $\dot{m}_{f,tot} = \dot{m}_f N_{stage} = 7.5 \times 2 \simeq 15$ mL min^{-1} for two stages, and $\dot{m}_{f,tot} = \dot{m}_f N_{stage} = 4 \times 4 \simeq 15$ mL min^{-1} for a four stages). These per-stage values were adopted for all subsequent analyses of CF_{H-R}.

The contribution of each stage to the total specific distillate productivity is shown in Fig. 6b. As in *CF*, the first stage (counted from top to bottom) provides the largest contribution to overall productivity. Indeed, Fig. 6c shows that both the mean membrane temperature and the mean transmembrane temperature difference decrease progressively from the first to the last stage. This combined decline accounts for the systematically lower productivity observed in downstream stages. However, unlike *CF*, the productivity of the first stage decreases as additional stages are installed, declining from approximately 0.8 kg m^{-2} h^{-1} in the single-stage configuration to about 0.63 kg m^{-2} h^{-1} in the four-stage case.

The underlying mechanisms are more complex than in *CF*. In CF_{H-R}, as discussed, the optimal mass flow rate varies significantly with the number of stages (Fig. 6a), leading to larger differences in salt concentration across configurations compared to *CF*, where the optimal mass flow rate remains constant. Thus, the behavior is influenced by two factors: temperatures and salt concentration. Regarding temperature, the mean membrane temperature $\overline{T_m}$ related to the first stage increases from approximately 72.1 °C in the single-stage configuration to 79.3 °C in the four-stage configuration (see Fig. 6c), while the mean transmembrane temperature difference $\overline{\Delta T_m}$

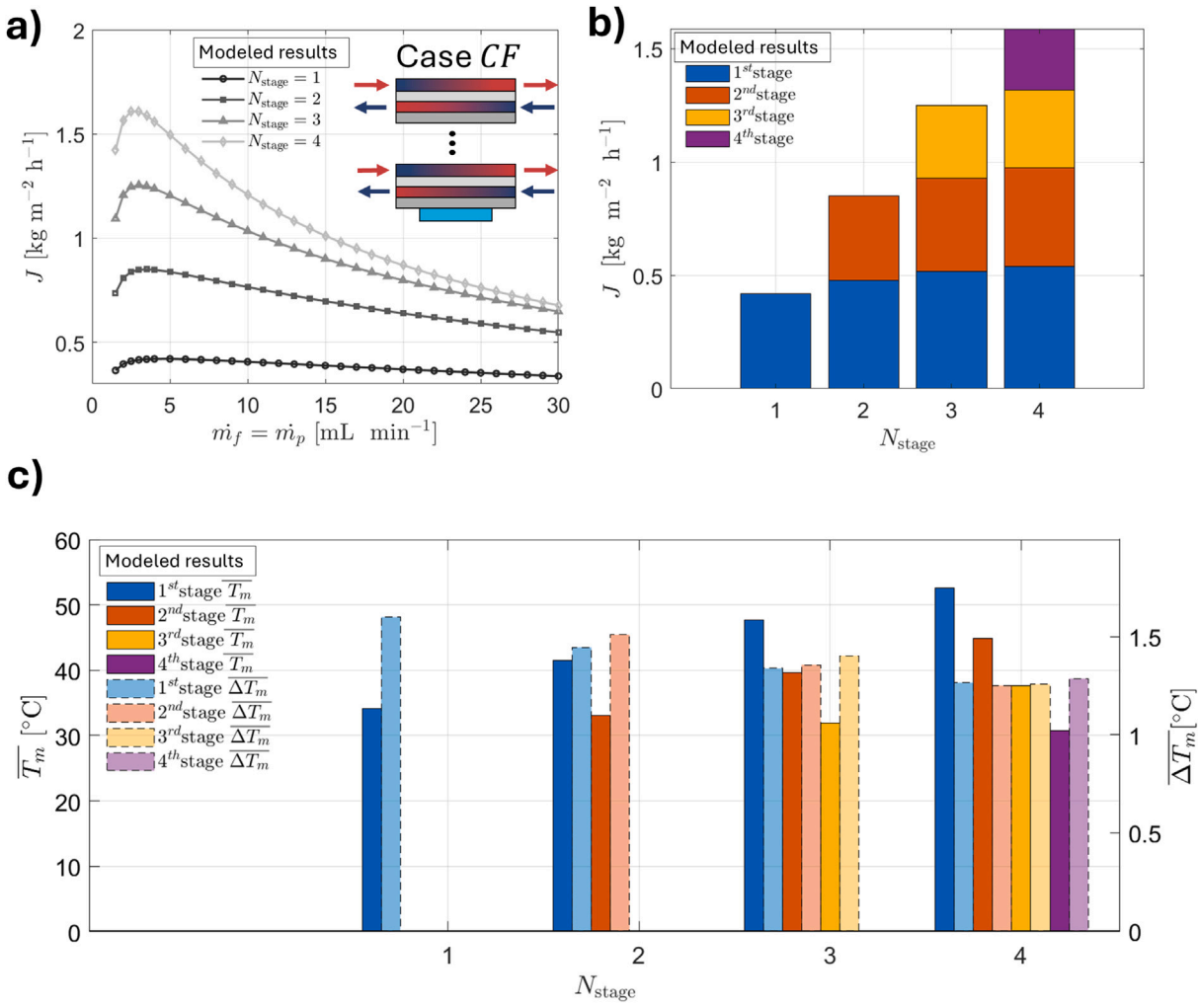


Fig. 5. Summary of the numerical results for the CF configuration. Simulations were performed under reference operating conditions: heating flux of 700 W m^{-2}, ambient heat transfer coefficient $U_{amb} = h_{air}$, inlet salinity of 35 g L^{-1}, and feed, permeate, ambient, and heat sink temperatures ($T_{f,in}$, $T_{p,in}$, T_{amb}, and T_{sink}) set to 20 °C. Equal feed and permeate mass flow rates ($\dot{m}_f = \dot{m}_p$) were imposed for each stage, and the heat sink overall heat transfer coefficient was fixed at U_{sink} = 125 W m^{-2} K^{-1}. (a) Total specific distillate productivity J (kg m^{-2} h^{-1}) vs. mass flow rate for different numbers of stages; different gray symbols correspond to a specific stage number. (b) Total specific distillate productivity vs. number of stages, with stacked bars showing individual stage contributions ($\dot{m}_f = \dot{m}_p$ = 3.5 mL min^{-1}). (c) Mean membrane temperature ($\overline{T_m}$, solid bars, left y-axis) and mean transmembrane temperature difference ($\overline{\Delta T_m}$, dashed transparent bars, right y-axis), both averaged along the module, for different multistage configurations.

related to the first stage decreases from about 1.13 °C to 1.07 °C (see Fig. 6c). Regarding salt concentration, the outlet concentration of the first stage increases as the number of stages rises, from 41.1 g L^{-1} in the single-stage configuration to 62.7 g L^{-1} in the four-stage configuration. Together, these effects explain the reduction in first-stage productivity with increasing stage number: as the optimal mass flow rate decreases and the temperature becomes more uniform, the impact of salt accumulation becomes increasingly significant.

Despite this redistribution of productivity among stages, the overall performance of CF_{H-R} remains consistently higher than that of CF. This improvement highlights the potential of the self-contained configuration, with internal heat recovery, to achieve higher performance by operating at higher temperature. However, the relative performance gain decreases as the number of stages increases. For the one-stage configuration, the improvement over the base case (i.e., CF) is approximately 91%, whereas for four-stage configuration it drops to about 19%.

3.5. Feed and permeate mass flow rate optimization: extrapolation and literature comparison

In the analyses presented so far, the feed and permeate mass flow rates were assumed equal ($\dot{m}_f = \dot{m}_p$). However, in distributed-heating systems, there is no fundamental requirement to enforce this constraint. The validated numerical model was therefore coupled with an optimization algorithm to determine the optimal $\dot{m}_f$ for different $\dot{m}_p$ values, for different solar irradiation values, number of stages, and system configuration.

The optimization was conducted over a mass flow rate range of 0.5–100 mL min^{-1} for both feed and permeate streams, with a resolution of 0.5 mL min^{-1}. Configurations comprising one to seven stages were analyzed under heat fluxes of 500, 700, and 1000 W m^{-2}, using artificial seawater at a salinity of 35 g L^{-1}. The inlet temperatures ($T_{f,in}$ and $T_{p,in}$), ambient temperature (T_{amb}), and heat sink temperature (T_{sink}, for CF only) were fixed at 20 °C. A membrane porosity of 0.825 and a thickness of 0.18 mm were assumed.

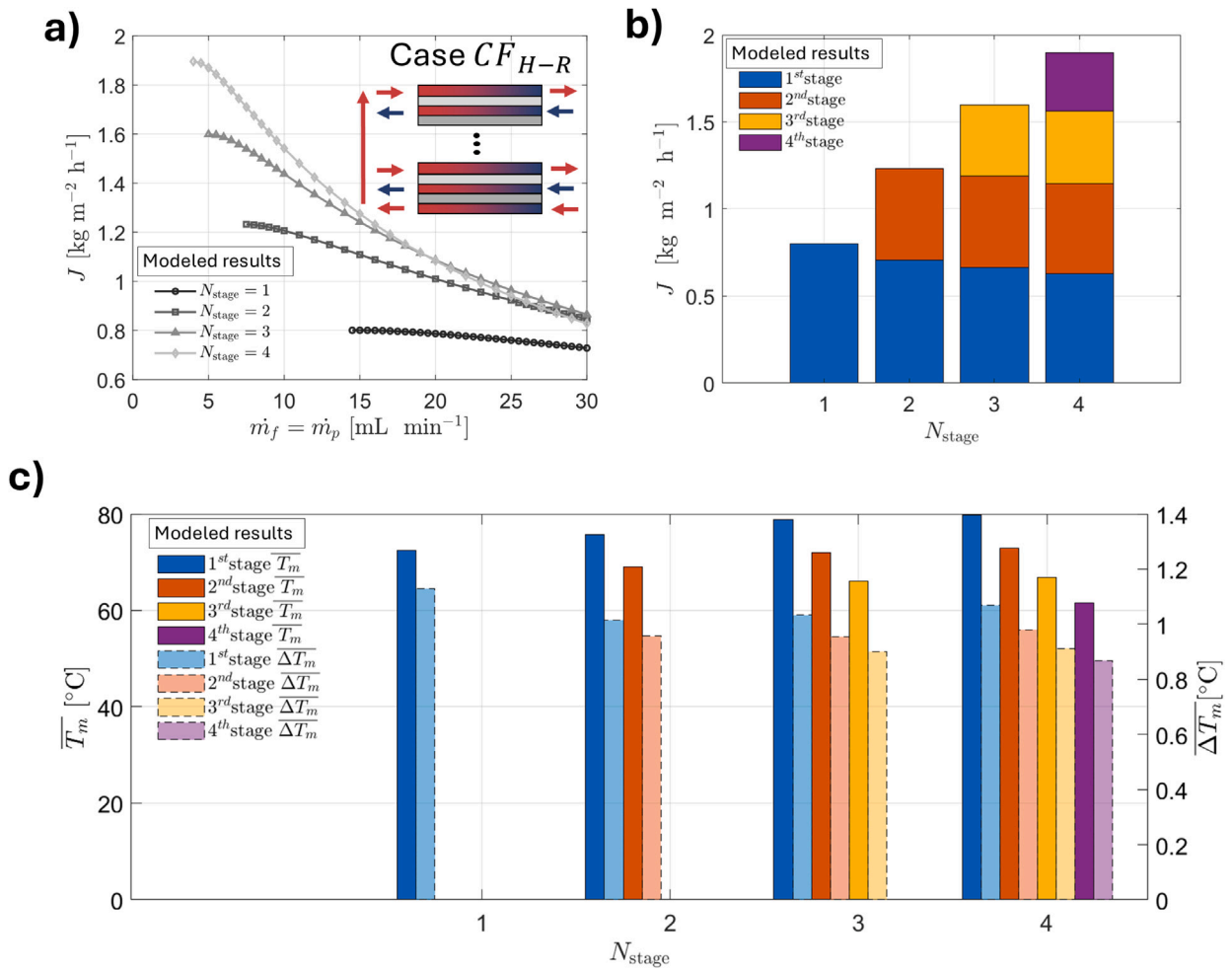


Fig. 6. Summary of the numerical results for the CF_{H-R} configuration with no external cooling. Simulations were performed under reference operating conditions: heating flux of 700 W m^{-2}, ambient heat transfer U_{amb}= h_{air}, inlet salinity of 35 g L^{-1}, and feed, permeate, ambient, and heat sink temperatures ($T_{f,in}$, $T_{p,in}$, T_{amb}, and T_{sink}) set to 20 °C. Equal feed and permeate mass flow rates ($\dot{m}_f = \dot{m}_p$) were imposed for each stage, with minimum values adjusted according to the number of installed stages: 14.5, 7.5, 5, and 4 mL min^{-1} for one- to four-stage configurations, respectively. (a) Total specific distillate productivity J (kg m^{-2} h^{-1}) vs. mass flow rate for different numbers of stages; different gray symbols correspond to a specific stage number. (b) Total specific distillate productivity versus number of stages, with stacked bars showing individual stage contributions ($\dot{m}_f = \dot{m}_p$ = 15, 7.5, 5, and 4 mL min^{-1} for one- to four-stage configurations). (c) Mean membrane temperature ($\overline{T_m}$, solid bars, left y-axis) and mean transmembrane temperature difference ($\overline{\Delta T_m}$, dashed transparent bars, right y-axis), both averaged along the module, for different multistage configurations.

To visualize the influence of feed and permeate mass flow rates on performance, three-dimensional parametric maps of the specific distillate productivity J are shown in Fig. 7. For clarity and compactness, representative cases are reported: one-stage and three-stage configurations for both CF and CF_{H-R} under 700 W m^{-2}. These capture the general trends without overloading the figure with all possible combinations. The color scale represents the maximum temperature within the computational domain, highlighting operational trade-offs associated with the 85 °C temperature constraint. These maps enable identification of the optimal operating regions for both configurations.

A general outcome of the optimization is that, for both CF and CF_{H-R}, maximum specific productivity is typically achieved at the minimum permeate mass flow rate ($\dot{m}_p$ = 0.5 mL min^{-1}), corresponding to the lower bound of the investigated range. Increasing $\dot{m}_p$ enhances advective cooling along the streamwise direction, thereby reducing the heat flux transferred from upper to lower stages and lowering the mean temperature throughout the module. Although a higher $\dot{m}_p$ slightly increases the mean transmembrane temperature difference, this effect is fully offset by the reduction in mean temperature, resulting in lower vapor flux.

Exceptions arise at high stage numbers and high heat fluxes, where additional cooling is required to prevent the maximum temperature from exceeding 85 °C. In such cases, the optimal $\dot{m}_p$ increases above the minimum value but remains below 4 mL min^{-1}. Overall, the optimal permeate mass flow rate in all investigated cases lies between 0.5 and 4 mL min^{-1}.

In contrast, the optimal feed mass flow rate ($\dot{m}_f$) differs substantially between CF and CF_{H-R}, reflecting distinct performance-limiting mechanisms.

In CF, where the maximum temperature is controlled by an external heat exchanger, the optimal $\dot{m}_f$ ranges between 2.5 and 6 mL min^{-1}, depending on stage number and heat flux. At suboptimal low flow rates, the produced vapor represents a larger fraction of the feed stream, leading to stronger solute accumulation, reduced water activity, and lower vapor pressure. Conversely, excessively high flow rates reduce the temperature gradient across the membranes, limiting vapor transport. For example, in the three-stage configuration, the optimal $\dot{m}_f$ increases from approximately 2.5 mL min^{-1} at 500 W m^{-2} to 4.5 mL min^{-1} at 1000 W m^{-2}. This reflects the higher thermal input, which enhances evaporation and solute accumulation, thereby requiring greater flow to mitigate concentration polarization.

The situation differs markedly for CF_{H-R}, where thermal regulation relies solely on the circulating mass flow rate. Here, temperature

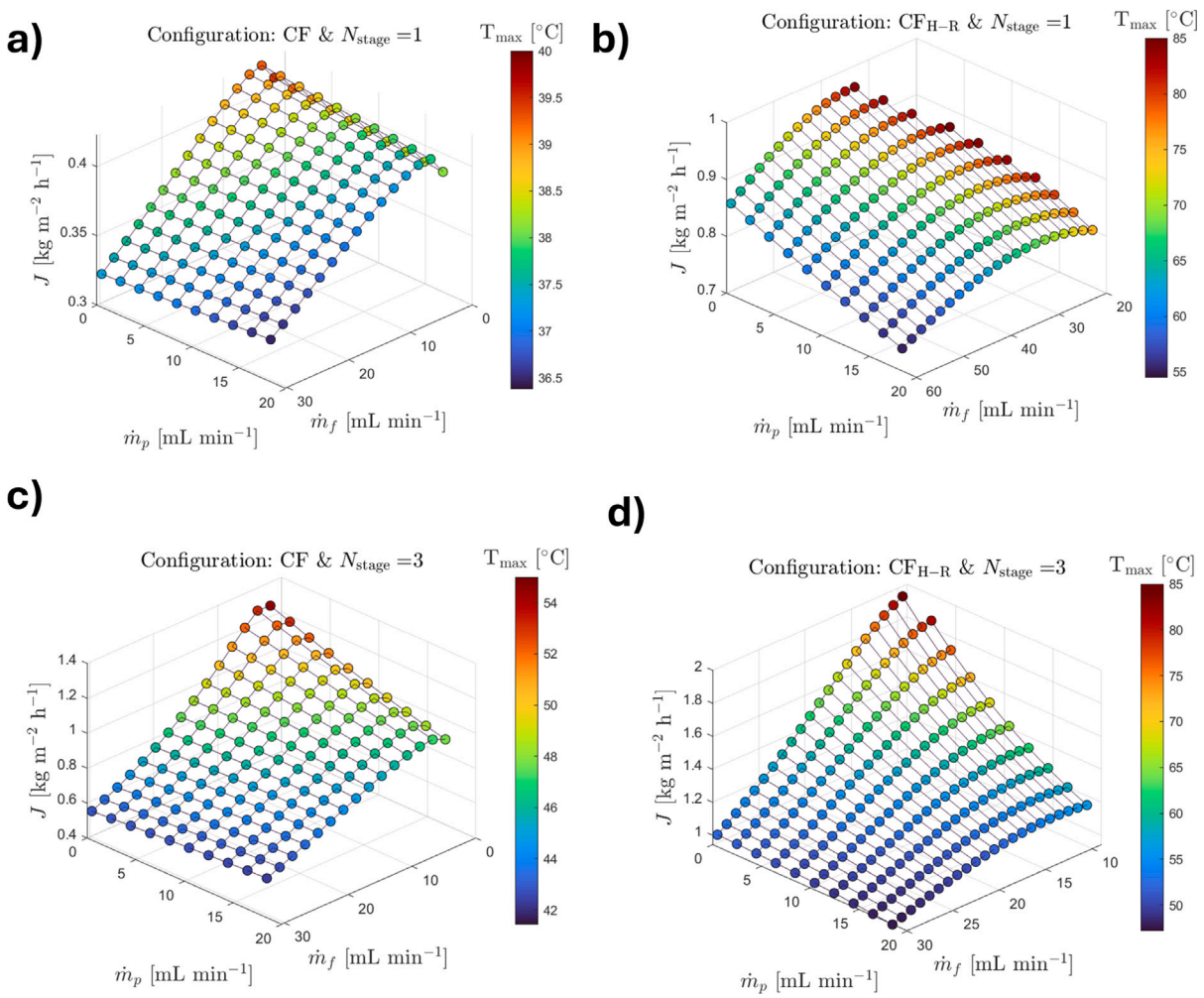


Fig. 7. Modeled device performance: three-dimensional parametric maps of system performance as a function of the per-stage feed and permeate mass flow rates ($\dot{m}_f$ and $\dot{m}_p$). Simulations were performed under reference operating conditions: heating flux of 700 W m^{-2}, artificial seawater salinity of 35 g L^{-1}, membrane thickness of 0.18 mm, membrane porosity of 0.825, and inlet feed, permeate, and ambient temperatures ($T_{f,in}$, $T_{p,in}$, T_{amb}) set to 20 °C. Panels (a) and (c) correspond to CF (one-stage and three-stage configurations, respectively), while panels (b) and (d) correspond to CF_{H-R} (one-stage and three-stage configurations, respectively). Only representative cases are shown for clarity. The z-axis represents the specific distillate productivity, J, while the color scale indicates the maximum temperature within the computational domain. These maps highlight the optimal operating regions and illustrate the trade-off between productivity and thermal constraints, complementing the derivative-based optimization analysis.

polarization is the dominant limitation, and excessively low flow rates can lead to uncontrolled temperature increases. Simulations exceeding the 85 °C threshold were therefore excluded. For the three-stage configuration, the optimal $\dot{m}_f$ increases from approximately 6.5 mL min^{-1} at 500 W m^{-2} to about 17 mL min^{-1} at 1000 W m^{-2}. This strong dependence reflects the need for enhanced convective cooling to preserve an effective temperature gradient across the membrane as thermal input rises. A notable advantage of this configuration is its adaptability to varying solar irradiance via flow-rate regulation, enabling stable performance over a wide operating range.

The overall optimization results for all configurations and operating conditions are summarized in Fig. 8a and b, which report the specific distillate productivity J and the thermal efficiency expressed as GOR, respectively.

Extrapolation to systems with up to seven stages enables assessment of scalability. For CF, productivity increases approximately linearly with the number of stages up to the fifth stage, after which a saturation effect becomes evident. At 700 W m^{-2}, a single stage produces 0.42 kg m^{-2} h^{-1}. Linear scaling would predict 2.52 kg m^{-2} h^{-1} and 2.94 kg m^{-2} h^{-1} for six and seven stages, respectively; however, optimized results yield 2.37 kg m^{-2} h^{-1} and 2.63 kg m^{-2} h^{-1}, indicating diminishing marginal gains. For CF_{H-R}, productivity deviates from linear scaling even at low stage numbers. Specific productivity increases from 0.97 kg m^{-2} h^{-1} (one stage) to 1.49 kg m^{-2} h^{-1} (two stages), corresponding to a 54% increase—well below linear behavior. The incremental gain decreases further with additional stages, dropping to approximately 11% between four and five stages and below 1% between six and seven stages. Beyond seven stages, only marginal improvements are expected.

As shown in Fig. 8, both configurations exhibit productivity saturation at high irradiation (1000 W m^{-2}) from the fifth to sixth stage onward. This behavior is primarily driven by the imposed 85 °C temperature limit. At high stage numbers, the first stage reaches this constraint, forcing operation at higher mass flow rates than those that would maximize productivity. The GOR follows a similar trend, reaching values between 150 and 200% at seven stages. Optimization also reveals a significant improvement at four stages. At 700 W m^{-2}, specific productivity increases from 1.59 kg m^{-2} h^{-1} (non-optimized reference case, Fig. 5) to 1.71 kg m^{-2} h^{-1} for CF, and from 1.89 kg m^{-2} h^{-1} (non-optimized reference case, Fig. 6) to 2.33 kg m^{-2} h^{-1} for CF_{H-R}.

To place the performance of the proposed device in context, Fig. 8c shows a comparison with the performance achieved by previously reported compact MD systems powered exclusively by distributed solar

energy and operated with feedwater at ambient temperature. The figure reports the specific productivity expressed in kg m^{-2} h^{-1} on the x-axis, while the vertical axis represents the absolute productivity expressed in g h^{-1}. This representation also provides information on device size, offering an indication of scalability. Three categories of devices are considered in the comparison, identified by different colors in the figure.

- First, passive capillary-driven solar MD systems (blue-colored symbols in Fig. 8c) consist of fully integrated absorber–membrane units in which feed delivery is governed by capillary action. Reported single-stage designs typically yield fluxes between 0.48 and 1.21 kg m^{-2} h^{-1} [25,47], whereas multistage configurations (up to ten stages) can attain values ranging from approximately 1.64 to 5.80 kg m^{-2} h^{-1} [25,30,47–50]. Among these, the device proposed by Xu et al. [47] reports the highest specific productivity in the literature, reaching 5.8 kg m^{-2} h^{-1}. Despite their promising specific performance, these systems are inherently constrained in size (generally ≤ 10–16 cm [31]) due to capillary flow limitations, which restrict overall throughput and limit scalability.
- Second, photothermal membrane distillation (PTMD) systems (orange-colored symbols in Fig. 8c) employ photothermal layers or nanostructured coatings to localize solar heating at the membrane–liquid interface, reducing temperature polarization and enhancing vapor generation. Most studies report specific productivities in the range of 0.3–0.77 kg m^{-2} h^{-1} [38,51,52]. Higher values have also been achieved, such as the 6.15 kg m^{-2} h^{-1} reported by Wu et al. [34] using a specialized photothermal coating. However, the corresponding absolute productivity remains relatively low (approximately 17.4 g h^{-1}) due to the limited effective membrane area of the device (28.3 cm^2). Furthermore, this class of prototypes often faces challenges related to coating durability, fabrication complexity, and scalability for large-area applications [53].
- Finally, a limited number of active compact MD systems, represented by green-colored symbols in Fig. 8c, have been proposed to overcome the size and flow limitations of passive configurations. These systems are conceptually aligned with the approach adopted in this work, with the results of the present study indicated by red symbols and the shaded red region in Fig. 8c. Early experimental studies investigated air-gap MD systems [40,54] with direct membrane heating, followed by developments in direct-contact MD configurations [55]. A key advantage of this approach is the elimination of external heat exchangers for heating, as thermal energy is absorbed and redistributed directly within the module. Despite these benefits, the literature on active compact MD systems remains relatively limited. Several studies are purely numerical or rely on vacuum-assisted operation [55], which introduces additional energy requirements. Available experimental demonstrations report fluxes on the order of 0.10–0.12 kg m^{-2} h^{-1} [40,55] under comparable operating conditions, with similar performance observed in recent compact air-gap MD prototypes using ambient-temperature feedwater. While these results confirm the feasibility of compact solar-driven MD, such systems often rely on gravity-driven permeate removal and precise control of module inclination, complicating large-scale implementation. A previous study by Morosanu et al. [42] identified a single-stage active configuration as the fundamental building block for the present work. That prototype achieved a specific productivity of 0.51 kg m^{-2} h^{-1}, an absolute production rate of 34.5 g h^{-1}, and a GOR of 18% with an active membrane area of $26 \times 26 = 676$ cm^2. The system proposed here represents a direct evolution of that prototype, with an increased effective area (1521 cm^2) and improved thermal management. As a result, the present study experimentally demonstrates a GOR of approximately 110%, an absolute production rate of 238.8 g h^{-1}, and a specific productivity of 1.57 kg m^{-2} h^{-1}. Furthermore, extrapolation based on the validated numerical model indicates a potential performance increase of up to approximately 200% with a corresponding $STEC$ of about 358 kWh_{th} m^{-3}, further supporting the improved thermal efficiency and the scalability of the proposed technology.

To complement the graphical comparison presented in Fig. 8c, Table 1 provides a structured summary of the main performance indicators and qualitative characteristics of the different MD system categories, highlighting the trade-offs between productivity, scalability, and system complexity.

4. Discussion and conclusions

This study investigated the performance of a multistage membrane distillation prototype powered by distributed solar energy. Two configurations (CF and CF_{H-R}) were analyzed through a combination of experimental campaigns and numerical simulations, followed by an optimization to identify optimal operating conditions. The main findings can be summarized as follows:

- CF configuration, when operating under the condition $\dot{m}_p = \dot{m}_f$, demonstrated a nearly linear increase in specific productivity (J) up to four stages, with a maximum observed experimental value of $J = 1.57$ kg m^{-2} h^{-1} and a gain output ratio (GOR) of approximately 110%. Experimental data closely matched numerical predictions (MAPE ~ 9%), confirming the reliability of the model.
- CF_{H-R} configuration, which does not rely on an external cooling heat exchanger, achieves higher productivity than CF. Furthermore, under equal feed and permeate mass flow rates ($\dot{m}_p = \dot{m}_f$), the single-stage configuration, with the implementation of an auxiliary channel, shows an improvement in terms of productivity and thermal efficiency, expressed in GOR of approximately 91%, whereas in the four-stage arrangement the relative gain decreases to about 16% (note that the mass flow rates differ between configurations to account for the staged thermal distribution). In this configuration, thermal management is entirely internal: the permeate from the last stage transfers heat to an auxiliary feed channel, preheating the feed before it enters the stages. The system's performance is strongly influenced by feed mass flow rates, as temperature polarization becomes the limiting factor in the absence of external cooling.
- The optimization analysis reveals that minimizing the permeate mass flow ($\dot{m}_p$) and adjusting the feed mass flow ($\dot{m}_f$) according to the number of stages and solar irradiance significantly enhances productivity for both configurations (CF and CF_{H-R}). For the four-stage configuration under 700 W m^{-2}, the optimized performance reaches $J = 1.71$–2.33 kg m^{-2} h^{-1} for CF and CF_{H-R}, respectively, corresponding to an improvement of 8%–23% compared to the reference condition ($\dot{m}_p = \dot{m}_f$). For single-stage configurations, the improvement is more limited, ranging between 1% and 20%, confirming the stronger impact of mass flow rate optimization in multistage systems.
- Extrapolation up to seven stages indicated saturation effects, with diminishing productivity gains beyond the fourth stage for CF and non-linear scaling for CF_{H-R}. Temperature constraints (85 °C) limit further scaling under high irradiance conditions. Overall, for the seven-stage configuration the predicted productivity ranges from approximately 1.5 to 4 kg m^{-2} h^{-1}, depending on configuration and operating conditions. These results suggest that configurations in the range of 4–6 stages provide a favorable compromise between performance gains, system complexity, and associated cost, while further increases lead to diminishing returns.

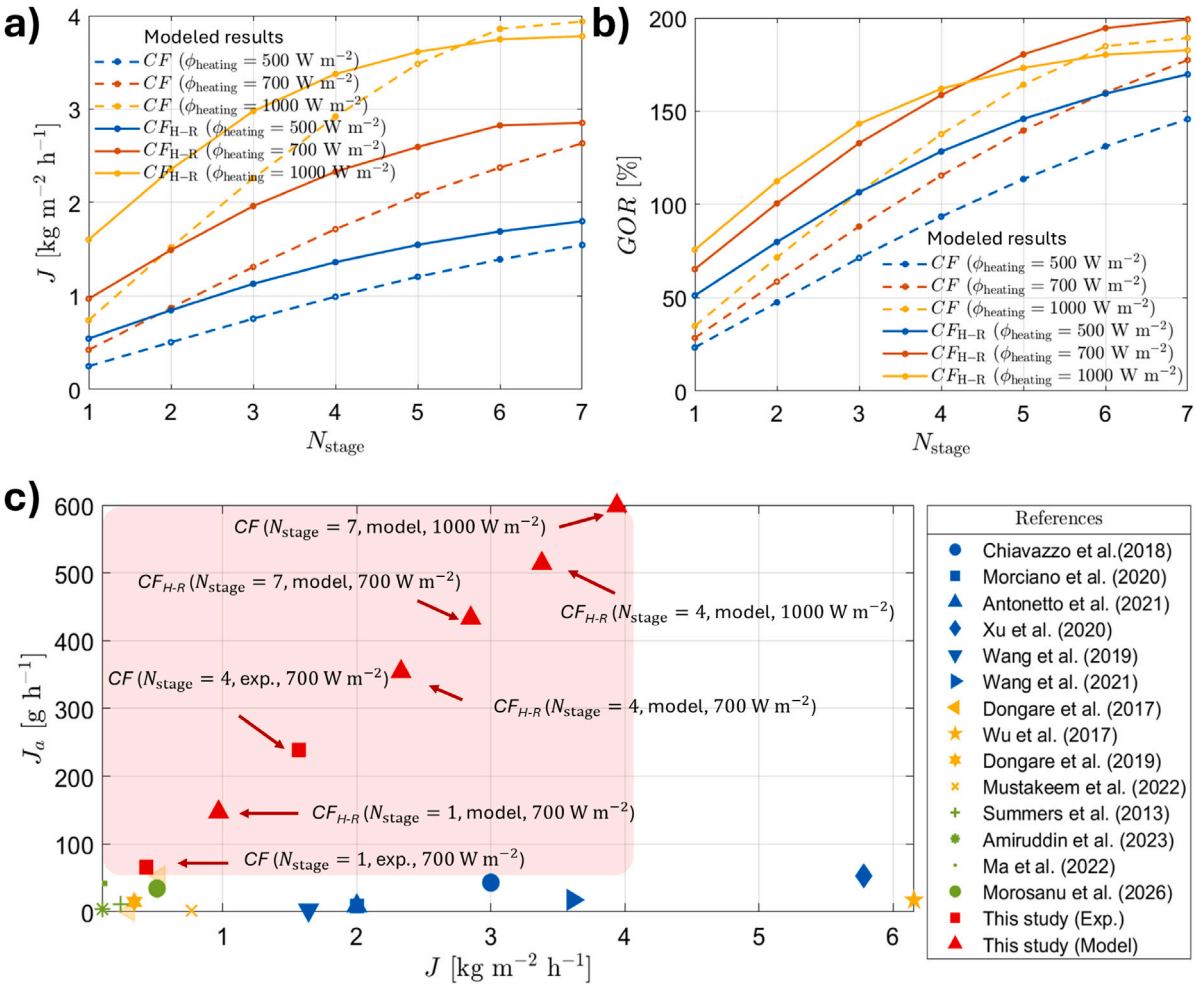


Fig. 8. Overview of the main results obtained using the gradient-based optimization framework to determine the optimal mass flow rates ($\dot{m}_f$ and $\dot{m}_p$) for heating fluxes between 500 and 1000 W m^{-2} and stage numbers from 1 to 7. Panels (a) and (b) report the optimized modeled performance of the system as a function of the number of installed stages and solar irradiance. Panel (a) shows the optimized specific distillate productivity J (y-axis) versus the number of stages (x-axis), while panel (b) presents the corresponding optimized gain output ratio (GOR). Colors indicate the heating flux, and solid and dashed lines correspond to CF_{H-R} and CF, respectively. All simulations were performed with inlet feed and permeate temperatures ($T_{f,in}$and $T_{p,in}$) and ambient temperature (T_{amb}) set to 20 °C, using artificial seawater with a salinity of 35 g L^{-1}, and a membrane thickness of 0.18 mm with a porosity of 0.825. Panel (c) compares the present results (experimental and modeled results for CF and modeled for CF_{H-R}, obtained by considering 700 and 1000 W m^{-2}; experimental and modeled results are identified as "Exp." and "Model.") with literature data: the x-axis represents the specific productivity (J) and the y-axis the absolute productivity (J_a). Marker colors indicate the type of system: passive (blue), photothermal active (yellow), other active systems (green), and this work (red). Red squares represent purely numerical results, and red circles correspond to experimental results.

Table 1
Comparison of different solar-driven MD system types with direct ambient-temperature feed heating, based on literature data, in terms of absolute productivity (J_a), specific productivity (J), and qualitative characteristics (advantages and limitations).

Type of the system	J_a [kg m^{-2} h^{-1}a]	J [kg m^{-2} h^{-1}]	Pros	Cons	Ref.
Passive	2.62–53.3	1.64–5.78	-High J -Simple design -No pumping required	-Geometry limitation -Low scalability due to capillarity	[25,30] [47,49] [48,50]
Photothermal active	0.85–53	0.3–6.156	-Localized heating -High J	-Membrane coating limits scalability	[51,52] [34,38]
Other active	4–42	0.1–0.51	-Medium scalability	-Low J	[40,54] [42,55]
Multistage active	65.4–599.3	0.43–3.94	-Medium/High scalability -High J_a	-Medium J	This work

- Compared with the literature, the proposed prototype achieves comparable specific productivity without relying on capillary-driven mass transport. This removes the size constraints typical of capillarity-based systems and enables significantly higher absolute productivity, reaching up to ~433.5 kg m^{-2} h^{-1}a for a seven stages at a distributed heat flux of 700 W m^{-2} (corresponding to 1 sun when heat losses are considered). This represents more than a sevenfold improvement over state-of-the-art systems based on extrapolated results. Considering only experimentally validated data, the four-stage prototype achieves an absolute productivity of ~238.8 kg m^{-2} h^{-1}, corresponding to an improvement of approximately 4.5× compared with the current state of the art. Furthermore, these results highlight the scalability of the proposed concept, as the actively circulated architecture enables multistage operation without the geometric constraints typical of capillary-driven systems and avoids the material and durability limitations associated with photothermal membrane coatings.

The analysis also provides several practical insights. Adjusting the feed and permeate flow rates offers a robust mechanism to control both productivity and thermal limits, enabling efficient operation under varying solar irradiance. Multistage designs further enhance energy utilization, although the optimal number of stages depends on the specific configuration and thermal management strategy. Moreover, in the CF_{H-R} configuration, the auxiliary feed channel enables internal heat recovery by preheating the incoming feed and reducing temperature polarization, thereby improving overall system efficiency without the need for external cooling. Overall, the proposed prototype demonstrates strong potential for scalable deployment, effectively overcoming key limitations of existing capillarity-based solar MD devices.

However, the inherent increase in feed salinity may raise concerns regarding scaling and fouling phenomena, particularly under prolonged operation. This aspect is widely recognized as one of the main challenges in MD systems, especially at high recovery ratios. In the present work, no deterioration in permeate quality was observed during the experimental campaign, although the analysis was limited to short-term operation. It is worth noting that the relatively low operating temperatures of the proposed system, compared to conventional thermal desalination processes, are expected to mitigate the propensity for inorganic scaling. In addition, the actively circulated configuration reduces concentration polarization and salt accumulation at the membrane surface, which are key drivers of fouling. More broadly, significant research efforts are currently being devoted to fouling mitigation in membrane distillation, particularly through the development of advanced membrane materials and surface modifications. These approaches are largely independent of the specific system configuration and can therefore be directly applied to the architecture proposed in this work. Nevertheless, long-term operation may still promote scaling, especially in the presence of sparingly soluble salts. In the context of decentralized and off-grid applications, this aspect is particularly relevant, as system robustness and maintenance requirements are critical factors. Based on the fouling mitigation strategies discussed by Warsinger et al. [56], dry-out conditions should be avoided when seawater is present inside the device, as they may promote salt crystallization on the membrane surface. In addition, periodic rinsing with clean water is recommended to mitigate salt accumulation and partially restore the initial distillate flux. Occasional chemical cleaning, for example using citric acid followed by NaOH, may also be adopted to recover membrane performance during prolonged operation. Future work will therefore focus on extended-duration testing under realistic conditions and on the integration of fouling mitigation strategies, such as optimized flow management, periodic flushing, or advanced membrane materials. In addition, material-level strategies aimed at improving thermal insulation and stability may further enhance the overall efficiency of the system, as suggested by recent studies on advanced composite materials for thermal management applications [57].

In conclusion, this work demonstrates that distributed solar-powered multistage membrane distillation can achieve high specific and absolute productivity while maintaining water quality and thermal efficiency, with strong potential for scalable deployment in decentralized and off-grid desalination applications. This makes the proposed approach particularly suited for practical implementation in contexts where simplicity, modularity, and independence from complex infrastructure are critical, providing a flexible solution adaptable to both local water supply strategies and scalable deployment scenarios. Future work will focus on experimental validation of larger stage configurations, long-term operation under realistic solar conditions, and integration with energy storage or phase-change materials to further improve system robustness and efficiency. Additional investigations will also explore alternative topological arrangements of the stages, such as series configurations, to assess their impact on thermal management and overall system performance.

Declaration of competing interest

The authors declare that they have no known competing financial interests or personal relationships that could have appeared to influence the work reported in this paper.

Acknowledgments

This work is part of the PNRR-NGEU project, funded by the Italian Ministry of University and Research (MUR) under Ministerial Decree No. 117/2023. The project has also been co-funded by Green Independence S.R.L., whose support is gratefully acknowledged.

Data availability

The data supporting the findings of this study are available at ZENODO and can be accessed at: https://zenodo.org/records/18242958.

References

[1] C. He, Z. Liu, J. Wu, X. Pan, Z. Fang, J. Li, B.A. Bryan, Future global urban water scarcity and potential solutions, Nat. Commun. 12 (1) (2021) 4667.
[2] E.R. Jones, M.F. Bierkens, M.T. van Vliet, Current and future global water scarcity intensifies when accounting for surface water quality, Nat. Clim. Chang. 14 (6) (2024) 629–635.
[3] S.N. Gosling, N.W. Arnell, A global assessment of the impact of climate change on water scarcity, Clim. Change 134 (3) (2016) 371–385.
[4] M. Kotb, M. Elboghdadi, M. Antar, M. Abido, A. Khalifa, Wind-powered multistage vacuum membrane distillation for sustainable water desalination, Appl. Therm. Eng. (2026) 130149.
[5] R.P. Barros, A. Fajardo, J. Lara-Borrero, Decentralized renewable-energy desalination: Emerging trends and global research frontiers—a comprehensive bibliometric review, Water 17 (14) (2025) 2054.
[6] Z.-F. He, C.-Y. Lai, H.-Y. Huang, Y.-H. Yang, D.-A. Le, Y.-H. Tu, T.-C. Wei, C.-C. Hu, Empowering remote communities: A portable, self-powered integrated desalination system, Desalination (2025) 119179.
[7] N.N. Phosha, X.G. Fuku, L. Tijing, M.M. Motsa, Exploring the application of solar irradiation in driving a stand-alone membrane distillation unit, Appl. Therm. Eng. 278 (2025) 127169.
[8] M.A. Al-Obaidi, S. Alsadaie, A. Alsarayreh, M.T. Sowgath, I.M. Mujtaba, Integration of renewable energy systems in desalination, Processes 12 (4) (2024) 770.
[9] M. Khashehchi, S. Thangavel, P. Rahmanivahid, M. Heidari, T. Moazzeni, V. Verma, A. Kumar, Solar desalination techniques: Challenges and opportunities, Highly Effic. Therm. Renew. Energy Syst. (2024) 305–329.
[10] A.K. Pandey, Sustainable water management through integrated technologies and circular resource recovery, Environ. Sci.: Water Res. Technol. 11 (8) (2025) 1822–1846.
[11] M.F. Hossain, The availability of global solar energy, in: Sustainable Global Development in Environment, Energy, Building, and Infrastructure, Springer, 2025, pp. 55–67.
[12] C. Lécuyer, Water on Earth: Physicochemical and Biological Properties, John Wiley & Sons, 2013.

[13] R. Venkatesh, Effect of hybrid nanofluid and polyethylene glycol/aluminium foam on thermal characteristics and energy storage performance of solar air heater, Appl. Therm. Eng. 291 (2026) 130213.
[14] M.R. Qtaishat, F. Banat, Desalination by solar powered membrane distillation systems, Desalination 308 (2013) 186–197.
[15] F. Han, H. Yu, J. Zhang, L. Xu, Harnessing tailored water states in hydrogels for low-enthalpy and high-efficiency membrane distillation, Appl. Therm. Eng. (2026) 130382.
[16] S. Shalaby, A. Kabeel, H. Abosheiasha, M. Elfakharany, E. El-Bialy, A. Shama, R.D. Vidic, Membrane distillation driven by solar energy: a review, J. Clean. Prod. 366 (2022) 132949.
[17] T. Arthur, G.J. Millar, E. Sauret, J. Love, Renewable hydrogen production using non-potable water: Thermal integration of membrane distillation and water electrolysis stack, Appl. Energy 333 (2023) 120581.
[18] G. Andrean, S. Bennett, H. Blanco, Global hydrogen review 2024, 2024.
[19] T. Arthur, G.J. Millar, J. Love, Thermal management of water electrolysis using membrane distillation to produce pure water for hydrogen production, J. Water Process. Eng. 67 (2024) 106255.
[20] M.M. Kabir, K.S. Im, L. Tijing, Y. Choden, S. Phuntsho, M.F.K. Mamun, G.M. Sabur, S.Y. Nam, H.K. Shon, Integrated membrane distillation-solid electrolyte-based alkaline water electrolysis for enhancing green hydrogen production, Desalination 601 (2025) 118580.
[21] D. Feng, L. Wang, Y. Chen, C. Su, Y.C. Woo, Z. Yang, Z. Wang, S. Lin, Highly-efficient seawater hydrogen production via a plug-and-play solar-powered membrane distillation-electrolysis system, Environ. Sci. Technol. (2026).
[22] N. Tukenmez, Y.E. Yuksel, M. Ozturk, Design and thermodynamic analysis of a solar-wind energy-based combined system for cleaner production of hydrogen with power, heating, hot water and clean water, Int. J. Hydrog. Energy 94 (2024) 256–277.
[23] C. Dang, Y. Cao, H. Nie, W. Lang, J. Zhang, G. Xu, M. Zhu, Structure integration and architecture of solar-driven interfacial desalination from miniaturization designs to industrial applications, Nat. Water 2 (2) (2024) 115–126.
[24] N. Lesniewska, M. Morciano, A. Tiraferri, M. Fasano, A comprehensive formalism for air-gap membrane distillation applied to the design of full-scale modules with direct solar heating, Desalination (2025) 119700.
[25] E. Chiavazzo, M. Morciano, F. Viglino, M. Fasano, P. Asinari, Passive solar high-yield seawater desalination by modular and low-cost distillation, Nat. Sustain. 1 (12) (2018) 763–772.
[26] M. Sajjad, M.A. Abdelsalam, A. Raza, F. AlMarzooqi, T. Zhang, Capillary pumping-evaporation modeling and experimental characterization of saline water transport for passive solar desalination, Int. J. Heat Mass Transfer 223 (2024) 125172.
[27] R.R. Meo, M. Morciano, Investigating the potentials and limitations of capillary-fed vapor generators: A heat and mass transfer study, Int. Commun. Heat Mass Transfer 137 (2022) 106309.
[28] R.R. Meo, M. Provenzano, M. Morciano, Investigating the solute concentration in capillary-fed vapor generators: A heat and mass transfer study, Int. Commun. Heat Mass Transfer 148 (2023) 106998.
[29] G. Vaartstra, L. Zhang, Z. Lu, C.D. Díaz-Marín, J.C. Grossman, E.N. Wang, Capillary-fed, thin film evaporation devices, J. Appl. Phys. 128 (13) (2020).
[30] M. Morciano, M. Fasano, S.V. Boriskina, E. Chiavazzo, P. Asinari, Solar passive distiller with high productivity and marangoni effect-driven salt rejection, Energy Environ. Sci. 13 (10) (2020) 3646–3655.
[31] V. Volkov, B. Bulushev, A. Ageev, Determination of the capillary size and contact angle of fibers from the kinetics of liquid rise along the vertical samples of fabrics and nonwoven materials, Colloid J. 65 (4) (2003) 523–525.
[32] A. Bamasag, E. Almatrafi, T. Alqahtani, P. Phelan, M. Ullah, M. Mustakeem, M. Obaid, N. Ghaffour, Recent advances and future prospects in direct solar desalination systems using membrane distillation technology, J. Clean. Prod. 385 (2023) 135737.
[33] M. Gao, C.K. Peh, F.L. Meng, G.W. Ho, Photothermal membrane distillation toward solar water production, Small Methods 5 (5) (2021) 2001200.
[34] J. Wu, K.R. Zodrow, P.B. Szemraj, Q. Li, Photothermal nanocomposite membranes for direct solar membrane distillation, J. Mater. Chem. A 5 (45) (2017) 23712–23719.
[35] A. Politano, P. Argurio, G. Di Profio, V. Sanna, A. Cupolillo, S. Chakraborty, H.A. Arafat, E. Curcio, Photothermal membrane distillation for seawater desalination, Adv. Mater. 29 (2) (2017) 1603504.
[36] S. Tian, X. Li, J. Ren, Z. Zhou, F. Wang, K. Shi, J. Xu, T. Gu, H. Shon, Emerging heat-localized solar distillation systems: Solar interfacial distillation vs photothermal membrane distillation, Desalination 572 (2024) 117147.
[37] J. Hu, G. Zhu, A. Ronen, D. Jassby, Q. Li, P. Wang, W. Wang, W. Zhang, Interfacial heating in membrane distillation: Advances, optimization strategies, and industrial applications for desalination, Environ. Sci. Technol. 59 (22) (2025) 10750–10769.
[38] P.D. Dongare, A. Alabastri, S. Pedersen, K.R. Zodrow, N.J. Hogan, O. Neumann, J. Wu, T. Wang, A. Deshmukh, M. Elimelech, et al., Nanophotonics-enabled solar membrane distillation for off-grid water purification, Proc. Natl. Acad. Sci. 114 (27) (2017) 6936–6941.
[39] P. Cheng, D. Wang, P. Schaaf, A review on photothermal conversion of solar energy with nanomaterials and nanostructures: from fundamentals to applications, Adv. Sustain. Syst. 6 (9) (2022) 2200115.
[40] D. Amiruddin, D. Mahajan, D. Fang, W. Wang, P. Wang, B.S. Hsiao, A facile ultrapure water production method for electrolysis via multilayered photovoltaic/membrane distillation, Energies 16 (15) (2023) 5765.
[41] M. Malaguti, M. Morciano, G. Viano, A. Achilli, A. Ali, C.A. Quist-Jensen, A. Tiraferri, Waste heat won't make membrane distillation cool: Thermodynamic analysis of cooling and pumping burdens, Desalination (2026) 120039.
[42] S. Morosanu, M. Morciano, Solar-driven membrane distillation with direct ambient-temperature feed heating: design, modeling, and experimental validation, Desalination 620 (2026) 119660.
[43] A.H. Al Hariri, A.E. Khalifa, Heat recovery of multistage circulated permeate gap membrane distillation for energy-efficient water production, Sep. Purif. Technol. 352 (2025) 128284.
[44] S.M. Alawad, D.U. Lawal, A.E. Khalifa, I.H. Aljundi, M.A. Antar, T.N. Baroud, M.M. Eltoum, Optimization and design analysis of multistage water gap membrane distillation for cost-effective desalination, Desalination 566 (2023) 116894.
[45] F. Incropera, D. DeWitt, T. Bergman, A. Lavine, Fundamentals of Heat and Mass Transfer, Wiley, 2007.
[46] A. Deshmukh, C. Boo, V. Karanikola, S. Lin, A.P. Straub, T. Tong, D.M. Warsinger, M. Elimelech, Membrane distillation at the water-energy nexus: limits, opportunities, and challenges, Energy Environ. Sci. 11 (5) (2018) 1177–1196.
[47] Z. Xu, L. Zhang, L. Zhao, B. Li, B. Bhatia, C. Wang, K.L. Wilke, Y. Song, O. Labban, J.H. Lienhard, et al., Ultrahigh-efficiency desalination via a thermally-localized multistage solar still, Energy Environ. Sci. 13 (3) (2020) 830–839.
[48] W. Wang, Y. Shi, C. Zhang, S. Hong, L. Shi, J. Chang, R. Li, Y. Jin, C. Ong, S. Zhuo, et al., Simultaneous production of fresh water and electricity via multistage solar photovoltaic membrane distillation, Nat. Commun. 10 (1) (2019) 3012.
[49] G. Antonetto, M. Morciano, M. Alberghini, G. Malgaroli, A. Ciocia, L. Bergamasco, F. Spertino, M. Fasano, Synergistic freshwater and electricity production using passive membrane distillation and waste heat recovered from camouflaged photovoltaic modules, J. Clean. Prod. 318 (2021) 128464.
[50] W. Wang, Y. Shi, C. Zhang, R. Li, M. Wu, S. Zhuo, S. Aleid, P. Wang, Solar seawater distillation by flexible and fully passive multistage membrane distillation, Nano Lett. 21 (12) (2021) 5068–5074.
[51] P.D. Dongare, A. Alabastri, O. Neumann, P. Nordlander, N.J. Halas, Solar thermal desalination as a nonlinear optical process, Proc. Natl. Acad. Sci. 116 (27) (2019) 13182–13187.
[52] M. Mustakeem, J.K. El-Demellawi, M. Obaid, F. Ming, H.N. Alshareef, N. Ghaffour, Mxene-coated membranes for autonomous solar-driven desalination, ACS Appl. Mater. Interfaces 14 (4) (2022) 5265–5274.
[53] A. Criscuoli, M.C. Carnevale, Localized heating to improve the thermal efficiency of membrane distillation systems, Energies 15 (16) (2022) 5990.
[54] E.K. Summers, et al., Experimental study of thermal performance in air gap membrane distillation systems, including the direct solar heating of membranes, Desalination 330 (2013) 100–111.
[55] Q. Ma, A. Ahmadi, C. Cabassud, Comparative study of small-scale flat-plate direct contact membrane distillation and vacuum membrane distillation modules with integrated direct solar heating, Desalination 529 (2022) 115633.
[56] D.M. Warsinger, J. Swaminathan, E. Guillen-Burrieza, H.A. Arafat, et al., Scaling and fouling in membrane distillation for desalination applications: a review, Desalination 356 (2015) 294–313.
[57] R. Venkatesh, Silicon carbide embedded polyester composite enriched by kevlar fiber via compression mould: performance study, J. Inst. Eng. (India): Ser. D (2024) 1–6.